COMPARISON OF THE EVAPORATION AND CONDENSATION HEAT TRANSFER COEFFICIENTS ON THE OUTSIDE OF SMOOTH, MICRO FIN AND VIPERTEX 1EHT ENHANCED HEAT TRANSFER TUBES

Kukulka D. J.[1]* , Smith R[2]. Li, W.[3] and Niu Z.[4]
[1]*Author for correspondence
Department of Mechanical Engineering Technology,
State University of New York College at Buffalo,
Buffalo, New York 14222,
USA,
E-mail: kukulkdj@buffalostate.edu
[2]Vipertex, Buffalo New York, USA
[3] Zhejiang University, PR China
[4]Fortune Group Co Ltd, PR China

ABSTRACT

An experimental investigation was performed to evaluate condensation and evaporation heat transfer on the outside of a smooth tube, herringbone micro fin tube and the Vipertex 1EHT enhanced heat transfer tube as a function of mass flux. Heat transfer enhancement is an important factor in obtaining energy efficiency improvements in two phase heat transfer applications. Utilization of enhanced heat transfer tubes is an effective enhancement method that is utilized in the development of high performance thermal systems. Vipertex™ enhanced surfaces have been designed and produced through material surface modifications, creating flow optimized heat transfer tubes that increase heat transfer. Heat transfer processes that involve phase-change processes are typically efficient modes of heat transfer; however current energy demands and the desire to increase efficiencies of systems have prompted the development of enhanced heat transfer surfaces that can be used in processes involving evaporation and condensation.

Surface enhancement of the 1EHT tube is accomplished through the use of a primary dimple enhancement coupled with a secondary background pattern made up of petal arrays. Enhancement of the herringbone is accomplished through the use of microfins. Convective condensation heat transfer and pressure loss characteristics were investigated using R410A on the outside of: (i) a smooth tube (outer diameter 12.7 mm); (ii) an external herringbone tube (fin root diameter 12.7 mm); and (iii) the 1EHT tube (outer diameter 12.7 mm) for mass flux ranging from 8 to 50 kg/ (m^2 s); at a saturation temperature of 318 K; with an inlet quality of 0.8 and an outlet quality of 0.1. For these conditions, both the 1EHT tube, and the herringbone tube did not perform as well as the smooth tube. This was an unexpected result.

Additionally the study also included a determination of the evaporation heat transfer coefficients using R410A on the outside of the same three tubes. The nominal evaporation temperature was 279 K; for a mass flux that ranged from 10 to 40 kg/m^2 s; with an inlet quality of 0.1 and the outlet quality of 0.8. Excellent heat transfer performance is demonstrated by the 1EHT tube showing an enhancement ratio of approximately 1.4. Evaporation heat transfer coefficient enhancement values for the herringbone tube ranges from 1.5 to 2.2. For the considered conditions, both the herringbone and 1EHT tubes have higher pressure drops than smooth tubes.

Microfins, surface roughness and three dimensional enhanced surfaces are often incorporated on the surface of tubes in order to enhance heat transfer performance. Under many conditions, enhanced surface tubes can recover more energy and provide the opportunity to advance the design of many heat transfer products. Enhanced heat transfer tubes are widely used in refrigeration and air-conditioning applications in order to reduce cost and create a smaller application footprint. A new type of enhanced heat transfer tube has been created using dimples/protrusions with secondary petal arrays; therefore it is important to investigate the heat transfer characteristics of the new Vipertex 1EHT enhanced surface tube and compare it to other tubes.

INTRODUCTION

Recently, the study of enhanced heat transfer has received a good deal of attention due to increased demands by industry for heat exchange equipment that is less expensive to build and operate. Savings in materials and energy use provides a strong motivation for the development of improved methods of heat transfer. Additional motivation is discussed by Reay [1] where he states that “between 1900 and 1955 the average rate of global energy use rose from about 1 TW to 2 TW. From 1955 to 1999 energy use rose from 2 TW to about 12 TW.” In 2011 energy use rose to an estimated value of 17 TW; and it is currently above 20 TW; with future demand expected to increase at the same rate. Government legislation and specific energy conservation targets have been set for overall energy reduction on a national basis by many countries. Additionally, government incentives are available to reduce energy usage and environmental impact. Gough [2] points out that the recent nuclear disaster in Japan has prompted the Japanese government to take a more active role in its serious drive to reduce energy use. Recently, additional countries have also started to adopt that approach, making the development of enhanced heat transfer even more important. Reay [1] notes

"that there is a need to reduce CO_2 emissions by over 50% in order to stabilize their impact on global warming. One way in which we can address this is by judicious use of process intensification technology." He goes on to define process intensification as: ''Any engineering development that leads to a substantially smaller, cleaner, safer and more energy-efficient technology." It is most often characterized by a huge reduction in plant volume; in addition "its contribution in reducing greenhouse gas emissions may also be significant." Heat transfer enhancement plays an important part in process intensification.

Cooling system designs used in the transportation and aerospace industries require that the heat exchangers are compact and lightweight. Additionally, heat transfer enhancement is very important for power plant, chemical, and oil/gas applications. This has led to the use and development of enhanced heat transfer surfaces. In general, enhanced heat transfer surfaces can be used to: (i) reduce the overall volume of the heat exchanger, making a heat exchanger compact and lightweight; (ii) reduce pumping power; (iii) increase the overall UA value of the heat exchanger (where U is the overall heat transfer coefficient and A is the heat transfer area); and (iv) reduce the initial cost of the heat exchanger. A higher UA value can obtain an increased heat exchange rate for fixed fluid inlet temperatures; or reduce the mean temperature difference for the heat exchanger (increasing the thermodynamic process efficiency and saving operating costs).

Enhancement techniques can be separated into two categories: passive and active. Passive methods require no direct application of external power to increase heat transfer and they may employ special surface geometries or fluid additives which produce a heat transfer enhancement. Active methods require external power for operation. The majority of commercial enhancement techniques are passive ones since active commercial techniques are costly and for some arrangements may be difficult to operate. Passive techniques provide enhancement by establishing a higher hA per unit base surface area (where h is the heat transfer coefficient and A is the heat transfer surface area). They are implemented by: (i) Increasing the effective heat transfer surface area without appreciably changing the heat transfer coefficient; (ii) Increasing the heat transfer coefficient without appreciably changing the surface area. This is typically accomplished by using enhanced heat transfer surfaces which provides mixing due to secondary flows and boundary-layer separation; and (iii) Increasing both the surface area and the heat transfer coefficient.

When looking at a modified surface geometry that is used to enhance heat transfer in an industrial heat exchange application there are various options to consider. In order to compare the performance, the heat transfer improvement produced by the enhanced surface is compared to the heat transfer performance produced using a smooth surface. An additional consideration is the increased pressure drop that is produced using the enhanced surface. Sometimes, the benefits gained from heat transfer enhancement are not great enough to offset the increase in friction. The performance goal for designs using enhancement techniques is the desire to gain maximum enhancement of heat transfer with a minimization of the pumping power.

Many previous studies have evaluated the enhancement of evaporators /condensers and the use of high performance components in various refrigeration/air-conditioning applications. These enhancement techniques include: twisted tape inserts, internal fins, and the use of enhanced surfaces [3]. In the late 1960s internal fins were first used in order to improve performance and decrease heat exchanger volume [3]; currently micro-fin tubes are widely used in many applications. Lavin and Young [4] were among the first to evaluate an internal fin tube, when they used R-12 and R-22 to evaluate evaporation in both horizontal and vertical tube orientations. Their results include a thorough discussion on the flow regimes that are produced using those enhanced tubes. Over the years there have been many more studies that discuss micro-fin tubes and a large knowledge base exists regarding the various heat transfer mechanisms; additionally accurate correlations are available to predict heat transfer and pressure drop [5, 6 and 7]. Tube parameters (i.e. fin shape, apex angle, helix angle, number of starts, fin height, etc.) produced on the surface of the heat transfer tubes all produce changes to the tubes performance and typically all parameters can be altered. Graham et al. [8] investigated condensation heat transfer performance for R134a in an axial fin tube with a 8.91 mm inside diameter; they found that the axial tube had a slightly better heat transfer performance than a smooth tube or an 18° helix tube. Fluid properties also affect tube performance; Yang and Webb [9] developed a model to predict the condensation heat transfer coefficient as a function of surface tension and vapor shear.

Devices inserted into channels can improve energy transport at a heated surface. Hong and Bergles [10] experimentally determined the heat transfer coefficient for laminar flow in a tube; they then went on to find a heat transfer coefficient enhancement ratio (ratio equal to approximately 9) when a twisted- tape was inserted in a tube. The enhancement ratio compares the heat transfer with the twisted tape to the heat transfer produced using an empty tube. Agarwal and Rao [11] evaluated the heat transfer enhancement coefficient for a plain circular tube with twisted tape inserts; for a wide range of conditions they found that the heat transfer coefficient enhancement ratio is approximately 1.21 to 3.70 times the h that is found in a plain tube. Liao and Xin [12] studied the heat transfer and friction characteristics inside tubes (with and without an internally enhanced, three-dimensional surface) using continuous or segmented copper twisted-tape inserts. They found that the compound enhanced tube (tube with a three-dimensional internal enhanced surface and a twisted-tape insert) provides the largest enhancement to the convective heat transfer coefficient.

Surface roughness is another method used to enhance heat transfer performance. Alam et al. [13] experimentally investigated the influence of surface roughness on the convective boiling heat transfer. Results of this study indicate that an increase of surface roughness will increase both the bubble nucleation site density and the heat transfer coefficient. Mahmoud et al. [14] investigated the effect of material surface roughness on the nucleate boiling heat transfer; they found that

the surface material type has a significant effect on the performance of *h* and conclude that brass performs the best.

Developing new configurations of enhanced micro-fin tubes (i.e. helix, cross-grooved, herringbone, three dimensional surfaces, etc.) is an effective approach that may be utilized in order to enhance the performance of heat exchangers. Compared to a smooth tube, the use of micro fin tubes can substantially improve the heat transfer performance with only a small pressure drop penalty. Therefore the use of enhanced surface tubes can make a heat exchanger more efficient and compact. Herringbone is a design of a micro-fin tube that, if properly designed and applied for a given set of conditions, it can produce a larger heat transfer coefficient (*htc*) than the *htc* produced by a helical micro-fin tube. Figure 1 shows the details of the enhanced outer surface, Vipertex herringbone tube that has been evaluated in this study. It has a pair of groove patterns which diverge at the bottom and converge at the top of the tube.

Previous studies have investigated the heat transfer enhancement on the inside of enhanced, micro-fin tubes. Miyara et al. [15] presents an early experimental study using R410A and discussed the flow patterns and enhancement mechanisms in herringbone tubes. Wellsandt and Vamling [16,17] carried out an in-tube evaporation investigation of R134a, R407C and R410A using a 4 m long, micro-fin herringbone tube (outer diameter of 9.35 mm) and compared the measured heat transfer and pressure drop data to previously reported correlations. Bandarra and Jabardo [18] studied convective boiling heat transfer and pressure drop of R134a in a (i) smooth; (ii) standard micro-fin and; (iii) herringbone copper tubes (9.52 mm external diameter). They found that the thermal performance of the herringbone tube is larger than that of a standard micro-fin tube over a large range of mass velocities. Additionally, the smallest heat transfer enhancements found in the herringbone tube occur at low velocities, with qualities larger than 50%. Finally, they found from their study that the herringbone tube has the highest pressure drop over the entire range of mass velocities and qualities. Afroz and Miyara [19,20] studied the pressure drop of single-phase, turbulent flows inside herringbone micro-fin tubes (several tubes with different fin dimensions) and proposed a generalized correlation (with an accuracy of ±10%) to predict the condensation pressure drop inside herringbone tubes. Cavallini et al. [21] presented a new relationship that predicts the condensation heat transfer coefficient in micro-fin tubes. Doretti et al. [22] presents a review of the condensation flow patterns inside smooth and micro-fin tubes. Olivier et al. [23] performed an experimental study to compare the heat transfer characteristics on the inside of a: (i) smooth; (ii) micro-fin and; (iii) herringbone tube.

Thome et al. [24] proposed the development of simplified flow structures in various in-tube flow regimes. Colombo et al. [25] presents heat transfer data and flow patterns for smooth and microfin tubes for evaporation and condensation conditions. Heat transfer coefficient and pressure drop of microfin tubes (with various fin geometries) are summarized. Performance varies depending on whether evaporation or condensation takes place. During evaporation, at low mass fluxes, all microfin tubes (independent of fin geometry) are particularly effective in increasing heat transfer and the performance of many of the tubes was similar. On the contrary, during condensation, the tube with the largest number of fins demonstrates the poorest performance; this is in agreement with the findings of other authors and to a certain extent with the current study. This suggests the existence of an optimal fin design in order to maximize heat transfer in condensation. The current study confirms the general trend for the outside of the tube, however previous studies of the same tube for flows inside the tube did not confirm the trend (additional tests are currently ongoing).

Zhang et al. [26] presents results from an experimental study on the evaporation heat transfer of R417A and finds the evaporation heat transfer coefficients using R417A were lower than R22 results; in addition the results for internally grooved tubes were lower than the results of smooth tubes for some conditions. Recently, Li et al. [27] discussed how internal surface enhancement can efficiently improve heat transfer under conditions of mixed convection. Grauso et al. [28] found that the local evaporation heat transfer coefficient of smooth tubes using R-134a is approximately 15% higher than those of R-1234ze(E) (low global warming potential (GWP) refrigerant), at low vapor qualities for smooth tubes. Del Col et al. [29] evaluated the condensation performance of grooved tubes, for low global warming potential (GWP) refrigerants (i.e. R1234ze(E)). They found that the condensation heat transfer coefficient for R1234ze(E) (for the same mass flux and saturation temperature) is lower than those of R32 and comparable with the condensation heat transfer coefficient of R134a. Mendoza-Miranda et al. [30] modelled a shell and tube evaporator with micro-fin tubes using R1234yf and R134a. Results of simulations indicate that the overall heat transfer coefficient of R1234yf is approximately 10% lower than that which is found for R134a. Some performance differences are seen in the use of low GWP refrigerants, with enhanced tubes for evaporation and condensation conditions. No conclusion on the performance of low GWP with the 1EHT tube can be made as part of this study; therefore additional heat transfer performance studies (for 1EHT enhanced tubes) using low GWP refrigerants are needed.

Shklover et al. [31] studied the condensing heat transfer of steam on the outside of smooth and low fin tubes. They found that performance on the finely finned tubes were not much better than the smooth tubes. The current study found the same trend since both enhanced tubes tested did not perform as well as a smooth tube. Ji et al. [32] used R134a to study condensing heat transfer on horizontal tubes with an enhanced surface structure. They performed an interesting comparison when they studied the performance as a function of the thermal conductivity of the tube. The four materials compared to copper were titanium, cupronickel (B10 and B30), and stainless steel. They go on to conclude that for the same enhanced structure, the tube made from a high thermal conductivity has an appreciably higher condensation heat transfer coefficient than the *htc* of a tube made from a low thermal conductivity material. Conclusions from [32] state that lower fin efficiency (resulting in a lower condensation heat transfer coefficient) is a result of the low tube material thermal conductivity. Tubes

made from a lower thermal conductivity material (with the same enhancement) may have a lower condensation heat transfer coefficient than similar tubes produced from a higher thermal conductivity material. Sajjan et al. [33] concludes from the results of their study that for external condensation heat transfer on a tube using iso-butane (R600a), that as the heat flux increases so does the wall sub-cooling. Yun et al. [34] investigated the external condensation heat transfer characteristics of R134a using stainless, integral-fin tubes. They found that the performance enhancement of the 19 fpi tube was much greater than that of the 26 fpi tube and conclude that this phenomenon can be explained by the effects of the condensate retention angle on the heat transfer coefficient at low condensate flow rates. Once again these results are similar to several previous results. Results from Zhao et al. [35] show that the condensation heat transfer coefficient increases by 9.79% when the superheating changes from 39.5 to 131.9 K. Meanwhile, the condensation heat transfer performance becomes worse due to the combination of condensation and natural convection as the cooling capacity inside the tube becomes smaller than the critical heat flux. Ribatski and Jacobi [36] presents a comprehensive literature review and discussed flow-patterns and how experimental parameters affect the evaporation heat transfer performance of plain and enhanced tubes. Additionally they provide information on tube bundle performance.

The 1EHT enhanced heat transfer tube, developed by Vipertex, is a novel kind of enhanced surface tube that was developed by modifying surface geometries [i.e. creating a modified surface that is a combination of large structures (dimples) and smaller patterns (petal arrays)] which can enhance the heat transfer coefficient on both the inside and outside surface of the tube; its details are shown in Figure 2a. The 1EHT enhanced heat transfer tube is neither a classic ‘‘integral roughness’’ (little surface area increase) tube, nor an internally finned tube (surface area increase with no flow separation). It can be considered to be more of a hybrid surface that increases surface area and produces flow separation from the dimpled protrusions on the tube. Surface enhancement structure is shown in Figure 2b. Enhancement of heat transfer using the 1EHT tube is produced from a combination of secondary flow generation, increased turbulence, boundary layer disruption, increased heat transfer surface area and an increased number of nucleation sites; all leading to an enhanced heat transfer performance for a wide range of conditions. So far little experimental work has been published on this kind of tube. Therefore the present study is important in order to better understand and advance the development of enhanced surface heat transfer tubes.

Kukulka et al. [37] studied enhanced heat transfer tubes for single phase heat transfer conditions. Additional work performed in Kukulka et al. [38] provides important information for the development of enhanced systems that may be exposed to fouling. They go on to discuss how these enhanced tubes increase heat transfer and also minimize the rate of fouling. Kukulka and Smith [39] evaluated the relationship of heat transfer enhancement to the surface geometry of 1EHT enhanced tubes. They compared the heat transfer for single phase flows and found that the 1EHT surface can produce heat transfer increases of more than 500% when compared to smooth tubes. Kukulka and Smith [40] present results for a bundle of 1EHT tubes showing an increase in the overall heat transfer coefficient up to 200% when compared to the heat transfer performance of a smooth tube bundle using typical fluids (n-Pentane, p-Xylene and water); for midpoint shellside Reynolds number values in the range of 2010 to 20,400; with effective mean temperature difference (EMTD) values between 8.6 ^{O}C and 65.7 ^{O}C. Kukulka et al. [41] performed an experimental investigation in order to determine the evaporation and condensation heat transfer coefficient of R22 and R410A inside the 1EHT tube for low flows. Guo et al. [42] performed an experimental investigation to evaluate convective condensation and evaporation of R22, R32 and R410A inside smooth and enhanced tubes. For condensation, the heat transfer coefficient of the herringbone tube is 2.0–3.0 times larger than a smooth tube and the 1EHT tube is 1.3–1.95 times that of the smooth tube. When considering evaporation, the 1EHT tube gives the best heat transfer performance for the three refrigerants considered; the heat transfer enhancement ratio (1.2–1.4) is larger than the inner surface area ratio (1.112). Those studies of the 1EHT and herringbone surface have provided the groundwork for the present study. No previously reported condensation or evaporation data exists for the 1EHT enhanced geometry considered in this study, therefore a comparison of 1EHT tube data will be made to smooth tube heat transfer results.

This study included an evaluation of the evaporation and condensation *htc* using R410A on the outside of a smooth tube, herringbone tube (outside enhanced micro-fin tube) and Vipertex 1EHT tube (all three tubes having an external diameter (OD) of 12.7 mm). As indicated in Wu et al. [43,44], helical micro-fin tubes are more effective at low mass fluxes due to the strong surface tension effects that are seen at low mass fluxes. Therefore, the focus of the current experimental investigation will be on low mass fluxes.

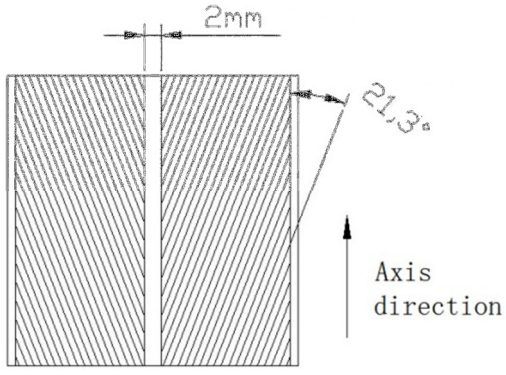

(a)

(b)

Figure 1 External Herringbone tube (a) Details of low fin enhancement (b) Outer surface enhancement structure

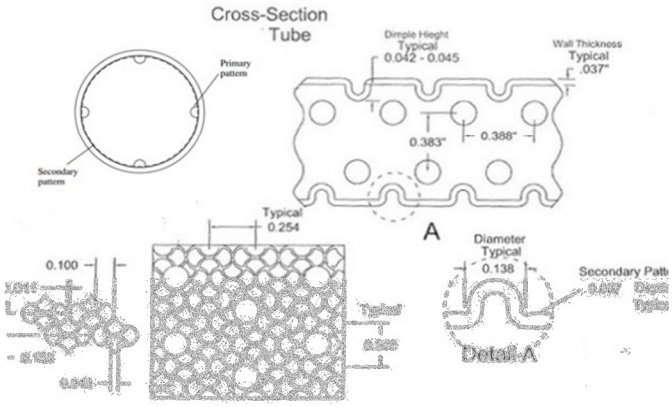

(a)

(b)

Figure 2 Vipertex 1EHT tube (a) Details of the primary enhancement structure with a typical diameter of 3.505 mm (0.138 in.) and a dimple height of 1.067 - 1.143 mm (0.042 - 0.045 in.), and secondary petal-shape patterns with a typical diameter of 2.54 mm (0.1 in.) and a typical height of 0.178 mm (0.007 in) (b) Outer surface enhancement structure

EXPERIMENTAL APPARATUS

An overall schematic of the experimental test apparatus that is used to evaluate the outside tube evaporation and condensation is showed in Figure 3a. It consists of two closed loops: (i) a R410A flow circuit which contains the test section, and (ii) a water circuit which can cool or heat the test section.

The refrigerant flow loop consists of a 50 L reservoir tank, digital gear pump with a variable speed motor, pressure regulating valve, mass flow meter, pre-heater, test section, condenser, and sight glasses. The regulating valve is used to control the mass flow rate through the refrigerant loop. In order to measure the refrigerant flow rate, a Coriolis Effect mass flow meter (with an accuracy of ±0.2% of the reading) located between the pump and the pre-heater is used. The sub-cooled liquid is electrically heated in the pre-heater and the required fluid inlet quality at the pre-heater outlet is produced; the fluid then enters the test section where it will be condensed or evaporated. Finally, the two-phase refrigerant is totally condensed and sub-cooled in a 9 kW, low-temperature bath (alcohol-water mixture) using a Platinum 100 RTD (with an accuracy of ±0.07 K) and a pressure transducer (with an accuracy of ±0.2%) that are located at the pre-heater inlet; the thermodynamic state of the fluid can then be determined The water circuit includes a centrifugal pump, water thermostat, control valve, and magnetic flow meter. The magnetic flow meter (with an accuracy of ±0.35% of reading) is used to determine the water flow rate in the annulus of the test section.

Figure 3b shows the straight, 2 m long horizontal test section that is part of the counter-flow, double-tube heat exchanger. Figure 3c shows the cross sectional view of the test section, including the inner test tube (i.e. smooth tube, herringbone tube and the 1EHT tube). The refrigerant flows in the annulus, on the outside of the tube. In order to heat the sample tube for evaporation testing, hot water flows inside the evaporation tube; otherwise cool water flows in the tube in order to condense the refrigerant on the outside of the tube. In order to minimize heat losses, the entire test facility is well insulated (especially the pre-heater and the test section). It is insulated using 40 mm thick foam insulation and 6 mm thick rubber insulation that creates a tight fitted enclosure. From the single-phase evaluation of R410A on the outside of the smooth tube, a heat balance of the test section was performed using the heat exchanged on the water side and the refrigerant side. The test section heat balance can be controlled to ±5%; indicating that the heat losses in the experimental apparatus can be ignored.

The inlet and exit refrigerant temperatures were measured using platinum RTDs that have been calibrated to an accuracy of ± 0.1^{O}C. Saturation pressure is measured using a pressure transducer at the inlet of the test section and a differential pressure transducer to measure the pressure drop across the test section. Heat transfer measurements are limited to average, rather than local values since the horizontal, annular design of the test section has measuring positions only at the inlet and outlet of the test section; additionally, pressure drop measurements are limited to total pressure drop for the entire test section. The refrigerant exits the test section and goes to a low temperature water bath, where the fluid is condensed and

sub cooled. The liquid refrigerant is recirculated through the system by a gear pump. Sub cooled liquid enters the pre-heater and the heated two-phase flow with a certain inlet quality exits at the pre-heater outlet. In order to determine the thermodynamic state of the fluid and enthalpy; readings from the platinum RTD and a pressure transducer located at the inlet of the pre-heater are used in their determination. Inlet vapor quality is calculated from an energy balance in the pre-heater and refrigerant vapor quality entering the test section was set by the pre-heater. The pre-heater was electrically and thermally insulated. Power supplied to the heaters was measured using watt transducers in order to find the total heat transferred.

The water loop consists of an annulus, centrifugal pump, magnetic flow meter, and a constant temperature water bath. The total heat transferred in the test section is determined from an energy balance for the water flowing through the annulus. A small wire, coiled outside the inner tube within a short distance of the annulus outlet, is used to stir the water. Its location and short length allows the acquiring of an accurate bulk water temperature at the exit. Heat flux was obtained from the inlet and exit water temperatures (measured using platinum RTDs). Flow rate is controlled by a valve located after the centrifugal pump. A detailed description of the test apparatus and uncertainty is given by Li et al. [45] and Wu et al. [43].

Three kinds of copper tubes were used in this experiment: (i) smooth tube; (ii) Vipertex 1EHT, a three dimensional enhanced (dimpled and textured), tube; and (iii) Viprtex herringbone tube. Lengths of all three tubes are 2 m. Smooth tube dimensions are: outer diameter, 12.7 mm; and inner diameter, 11.43 mm.

Data were collected when deviations (over 4 minutes) were below 0.1 K for temperature and 2 kg/m^2 s for mass flux. Heat flux was determined using the actual inner surface heat transfer area of the tube. Data was reduced to calculate the heat transfer coefficient.

Experimental heat transfer test conditions

Condensation heat transfer evaluation using refrigerant R410A was conducted at a saturation temperature of 45℃; for a mass flux range of 5 - 50 kg/(m^{2}s); heat flux range of 3 - 23 kW/m^2; 0.8 inlet quality and 0.1 outlet quality. Evaporation heat transfer evaluation using R410A was conducted at a nominal evaporation temperature of 6℃, with inlet and outlet qualities of 0.1 and 0.8. Mass flux ranged from 10 to 40 kg/m^{2}s.

Mass flux and heat flux varied in the experiments; with saturation temperature and inlet/ outlet quality being kept constant. Mass flux was calculated using the nominal annulus flow area, A_c. Heat flux was determined using the total outer surface heat-transfer area, A.

Experimental uncertainty

The uncertainty of the Platinum RTDs is ±0.1℃; uncertainty of the differential pressure transducers is ±0.05% of the set span; and the flow meter uncertainty is ±1.0% of the flow rate. Single-phase heat-transfer tests have been performed in order to verify the uncertainty in the heat transfer measurement. It was determined that the average heat transfer deviation between the water side and refrigerant side is 3.1%. Finally, the uncertainty of the heat transfer coefficient was determined to be ± 5.1%.

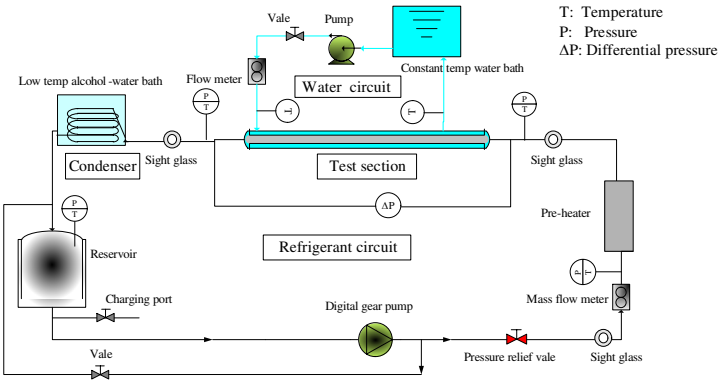

(a)

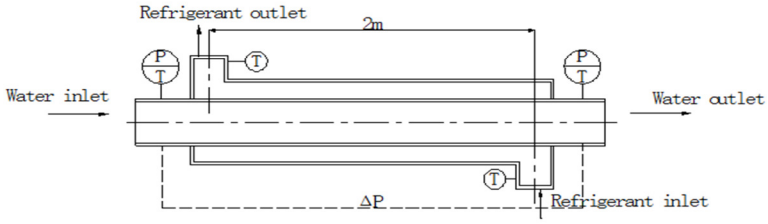

(b)

Figure 3 Schematic drawings of (a) Test rig and (b) Test section

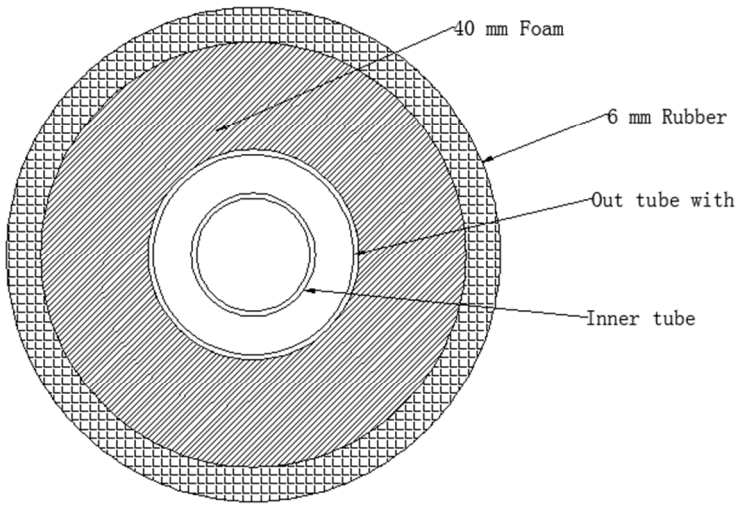

Figure 3c Cross sectional view of the test tube

Table 1 Uncertainty values of the primary measurements and dependent quantities.

Primary measurements		*Dependent quantities*	
Diameter	±0.05 mm	Mass flux, G, kg m^{-2} s^{-1}	±2.2%
Length	±0.2 mm	Heat flux, q, W m^{-2}	±4.3%
Temperature	±0.07 K	Vapor quality, x	±5.2%
Electric current	±0.01 A	Frictional pressure drop, ΔP_f	±3.9%
Electric voltage	±1.0 V	Heat transfer coefficient, h, W m^{-2} K^{-1}	±15.4%
Pressure, range: *0-40 bar*	±0.2% of full scale		
Differential Pressure, range: *0-100 kPa*	±0.05% of reading		
Water flow rate, range: *0-12 L* min^{-1}	±0.35% of reading		
Refrigerant flow rate, range: *0-60 kg* h^{-1}	±0.2% of reading		

DISCUSSION OF RESULTS

Figure 4 shows the variation of the Nusselt Number, Nu (based upon the determined outside condensation heat transfer coefficient) with Reynolds Number (Re), using R410A, on the outside surface of: (i) a smooth tube; (ii) the 1EHT tube; and (iii) a herringbone tube with an enhanced external surface. In a comparison of all three tubes, it was found unexpectedly that the smooth tube has the best condensation heat transfer coefficient for the conditions considered. Additionally, the heat transfer coefficient of the external herringbone tube is only approximately 60% of that determined for the smooth tube. The lowest heat transfer coefficient (over the range of mass flux) was found in the 1EHT tube; it was approximately 23% ~ 65% of the heat transfer coefficient found for the smooth tube.

Figure 4 shows that the condensation heat transfer of a smooth tube initially decreases and then gradually flattens out over the range of Re; for the external herringbone tube, the Nu decreases at first and then increases as Re becomes larger than 1500. Finally the Nu for the 1EHT tube increases as Re increases. Figure 5 presents the relationship between DP* (ratio of the pressure loss in the enhanced tube to the smooth tube pressure loss) and the Re. Pressure drop increases with increasing flows. All three tubes show the same trend in pressure drop, with the smooth tube showing the lowest pressure loss values. It appears that since the heat transfer coefficient of the 1EHT tube and the externally enhanced herringbone tube are lower than that of a smooth tube that perhaps the liquid drainage is worse for an enhanced surface at low mass flux values. A further study is needed to confirm the actual cause of this unexpected phenomenon.

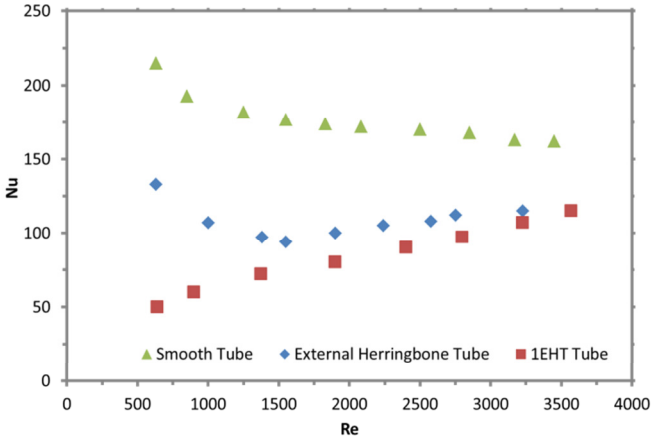

Figure 4 Comparison of Nusselt Number, Nu (based upon evaluated outside condensation heat transfer coefficient) as a function of Reynolds Number, Re for a (i) smooth; (ii) external herringbone; and (iii) 1EHT tube in R410a with a saturated temperature of 45 ^{O}C; with an inlet quality of 0.8 and outlet quality of 0.1

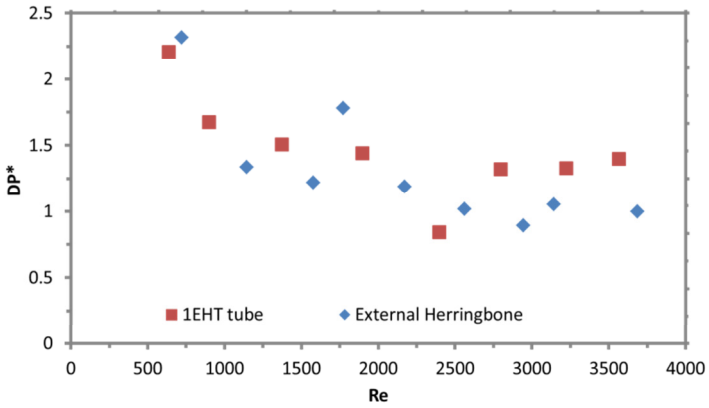

Figure 5 Comparison of DP* (ratio of enhanced tube pressure drop to the pressure drop in a smooth tube) under condensation as a function of Reynolds Number (Re) for a (i) external herringbone; and (ii) 1EHT tube in R410a with a saturated temperature of 45 ^{O}C; with an inlet quality of 0.1 and outlet quality of 0.8

Figure 6 shows the trend in the evaporation heat transfer when refrigerant R410A is used on the outside surface for a: (i) smooth tube; (ii) herringbone tube; and (iii) 1EHT tube. For each of the three tubes, the Nu (based upon the exterior surface evaporation heat transfer coefficient) typically increases with increasing Re. However an exception exists for the herringbone tube in the Re range of 750 to 1100; in this range the Nu decreases, eventually becoming only slightly larger than the Nu of the 1EHT tube for Re values larger than 1100. The herringbone tube has a larger *htc* at a lower mass flux; this has been discussed for micro fin tubes by Wu et al. [43,44].

Compared to a smooth tube, the herringbone tube presents a significant enhancement of the heat transfer coefficient for Re values to approximately 750, with the heat transfer enhancement ratio reaching a maximum of 2.2. However, as Re increases above 1100, the heat transfer enhancement decreases to an enhancement ratio in the range of 1.46 to 1.57.

The evaporation heat transfer coefficient of the 1EHT tube is larger than that of smooth tube; showing an increase in the heat transfer coefficient ratio values to 1.4. It is shown that the increase in the heat transfer coefficient is larger than the 1EHT heat transfer surface area ratio (1.112), making it a good tube for use in evaporation conditions.

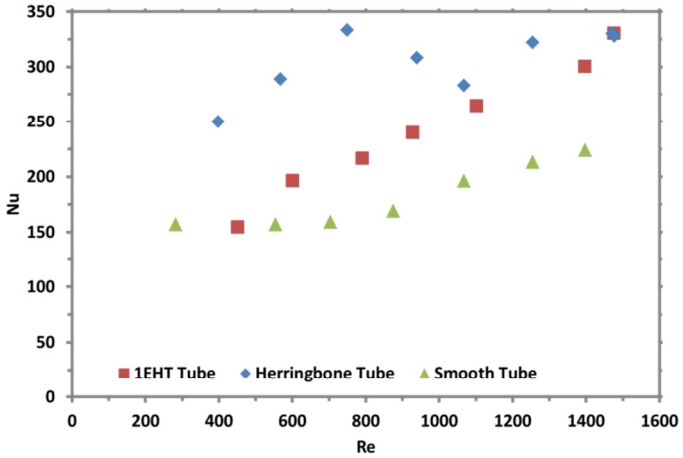

Figure 6 Comparison of Nusselt Number, Nu (based upon evaluated outside evaporation heat transfer coefficient) as a function of Reynolds Number, Re for a (i) smooth; (ii) external herringbone; and (iii) 1EHT tube in R410a with a saturated temperature of 6 ^{O}C ; with an inlet quality of 0.1 and outlet quality of 0.8

The pressure drop of the three tubes has a consistent trend that shows that the pressure drop increases with the mass flux; this trend is also presented in several other studies [16, 17, and 18]. Figure 7 shows the variation of DP* with Re, for the enhanced tubes tested. At higher flows, the 1EHT tube has the largest pressure drop among the three tubes; it is approximately 90% larger than that found in a smooth tube. Pressure drop of the herringbone tube is approximately 60% higher than the smooth tube.

The condensation/evaporation performance on the outside of a tube does not match the condensation/evaporation performance that is demonstrated on the inside of the tube, as shown in [41, 42]. Based upon current results and those found in [16] it can be concluded that for the same micro-fin geometries there will be a variety of influences on the heat transfer performance on the inside and outside of the tube. Therefore additional studies are needed to better understand these differences and the mechanism of enhancement.

CONCLUSIONS

Condensing heat transfer of R410a on the outside surface of a smooth tube, external herringbone tube and the 1EHT tube has been experimentally measured over a range of mass flux. The overall heat transfer coefficient was measured for a mass flux that ranged from 5 to 50 kg/m^2 s. In summary the major findings are:

(1) Condensation heat transfer coefficient of a smooth tube is higher than that of the 1EHT tube and the external herringbone tube for the mass flux range evaluated.

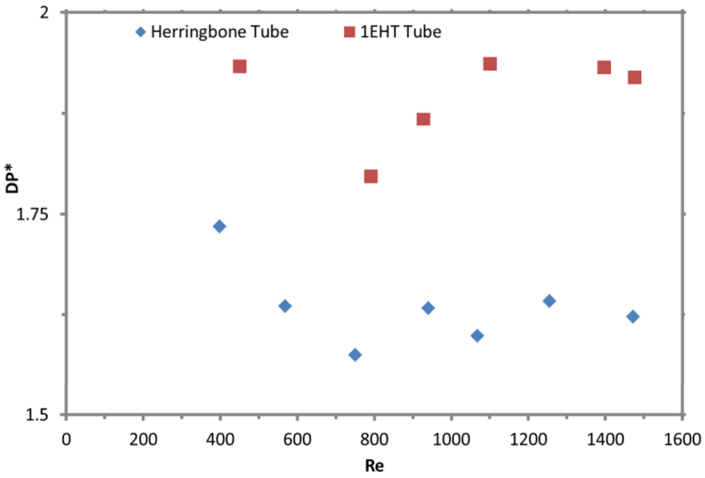

Figure 7 Comparison of DP* (ratio of enhanced tube pressure drop to the pressure drop in a smooth tube) under evaporation as a function of Reynolds Number (Re) for (i) external herringbone; and (ii) 1EHT tube in R410a with a saturated temperature of 6 ^{O}C ;with an inlet quality of 0.1 and outlet quality of 0.8

(2) Condensation heat transfer coefficient of the 1EHT tube increases over the mass flux range; while condensation heat transfer coefficient of the smooth tube decreases over the same range of mass flux. For the external herringbone tube, the condensation heat transfer coefficient decreases at first and then rises over the remaining range of mass flux. Heat transfer coefficient of the external herringbone tube is only approximately 60% of that determined for the smooth tube; while the 1EHT tube was approximately 23% ~ 65% of the heat transfer coefficient found for the smooth tube performance.

(3) There is little difference in the condensation pressure loss of the enhanced tubes over the Re range evaluated.

An experimental evaluation of evaporation (at other flow flux rates) on the outside surface of a smooth, herringbone and 1EHT enhanced surface tube has been conducted in this study. Experimental data was obtained at the evaporation temperature of 6 °C; for a refrigerant mass flux that ranged from 8 to 35 kg $m^{-2}s^{-1}$; inlet quality of 0.1 and outlet quality of 0.8. The objective of the study was to determine how the outside evaporation heat transfer coefficient varies with mass flow for each of the tubes.

Evaporation heat transfer coefficients of the herringbone tube and 1EHT tube are larger than that of the smooth tube; typically increasing with an increase in the mass flux. This is true for all three tubes, except for the herringbone tube at mass flows in the range from 17 to 25 kg/m^2. Compared to a smooth tube, the herringbone tube heat transfer enhancement ratio reaches a maximum of 2.2 and decreases to an enhancement ratio in the range of 1.46 to 1.57. The evaporation heat transfer coefficient enhancement ratio, for the 1EHT tube, ranges up to 1.4. Pressure drop increases with an increase to the mass flux for all three tubes. The performance trends demonstrated for inside condensation in Kukulka et al. [41] and Guo et al. [42], for the same enhanced structures (inside enhancement) are not found in the present study. This was unexpected and requires additional investigation.

In addition, studies are needed for a larger range of flow rates in order to determine if the trends found in this study continue. Additional studies are also required using low GWP refrigerants, other size tubes and other enhancement dimensions.

REFERENCES

[1] Reay D., The role of process intensification in cutting greenhouse gas emissions, *Applied Thermal Engineering*, 28, 2008, 2011–2019.

[2] Gough M. J., Process heat transfer enhancement to upgrade performance, throughput and reduced energy use, *Chemical Engineering Transactions*, 29, 2012, 1-6.

[3] Webb R. L., Kim Nae-Hyun, Principles of Enhanced Heat Transfer, 2nd edition, Taylor & Francis Group, New York, 2004.

[4] Lavin J. G., Young E. H., Heat Transfer to Evaporating Refrigerants in Two-Phase Flow, *AIChE Journal*, 11, 2004, 1124-1132.

[5] Kandlikar S.G., Raykoff T., Predicting flow boiling heat transfer of refrigerants in microfin tubes, *Journal of Enhanced Heat Transfer*. 4, 1997, 257-268.

[6] Del Col D., Webb R. Narayanamurthy R., Heat Transfer Mechanisms for Condensation and Vaporization inside a Microfin Tube, *Journal of Enhanced Heat Transfer*, 9(1) ,2002, 25-37.

[7] Zürcher O., Thome J. Favrat D., An Onset of Nucleate Boiling Criterion for Horizontal Flow Boiling, *International Journal of Thermal Sciences*, 39, 2000, 909-918.

[8] Graham D., Chato J. C., Newell T. A., Heat Transfer and Pressure Drop During Condensation of Refrigerant 134a in an Axially Grooved Tube, *International Journal of Heat and Mass Transfer*, 42, 1999, 1935-1944.

[9] Yang C. Y., Webb R. L., A Predictive Model for Condensation in Small Hydraulic Diameter Tubes Having Axial Micro-Fins, *Journal of Heat Transfer*, 119, 1997, 776-82.

[10] Hong S. W., Bergles A. E., Augmentation of Laminar Flow Heat Transfer in Tubes by Means of Twisted-Tape Inserts, *Journal of Heat Transfer*, 98, 1976, 251-6.

[11] Agarwal S. K., Rao M. R., Heat Transfer Augmentation for the Flow of a Viscous Liquid in Circular Tubes Using Twisted Tape Inserts, *International Journal of Heat and Mass Transfer*, 39, 1996, 3547-3557.

[12] Liao Q., Xin M. D., Augmentation of Convective Heat Transfer inside Tubes with Three-Dimensional Internal Extended Surfaces and Twisted-Tape Inserts, *Chemical Engineering Journal*, 78, 2000, 95-105.

[13] Alam T., Lee P. S., Yap C. R., Effects of Surface Roughness on Flow Boiling in Silicon Microgap Heat Sinks, *International Journal of Heat and Mass Transfer*, 64, 2013, 28-41.

[14] Mahmoud M.M., Karayiannis T. G., Kenning D., Surface Effects in Flow Boiling of R134a in Microtubes, *International Journal of Heat and Mass Transfer*, 54, 2011, 3334-46.

[15] Miyara A., Nonaka K., Taniguchi M., Condensation heat transfer and flow pattern inside a herringbone-type micro-fin tube, *International Journal of Refrigeration*, 23, 2000, 141-152.

[16] Wellsandt S. and. Vamling L, Evaporation of R407C and R410A in a horizontal herringbone microfin tube: heat transfer and pressure drop. *International Journal of Refrigeration*, 28(6), 2005, 901-911.

[17] Wellsandt S. and. Vamling L, Evaporation of R134a in a horizontal herringbone microfin tube: heat transfer and pressure drop. International Journal of Refrigeration-Revue *Internationale Du Froid*, 28(6), 2005, 889-900.

[18] Bandarra E.P. and Jabardo J.M.S., Convective boiling performance of refrigerant R-134a in herringbone and microfin copper tubes. *International Journal of Refrigeration-Revue Internationale Du Froid,* 29(1), 2006, 81-91.

[19] Afroz H.M.M. and Miyara A., Prediction of condensation pressure drop inside herringbone microfin tubes, *International Journal of Refrigeration*, 34, 2011, 1057-1065.

[20] Afroz H.M.M. and Miyara A., Friction factor correlation and pressure loss of single-phase flow inside herringbone microfin tubes. *International Journal of Refrigeration-Revue Internationale Du Froid*, 30(7), 2007, 1187-1194.

[21] Cavallini A., Del Col D., Mancin S., Rossetto L., Condensation of pure and near-azeotropic refrigerants in microfin tubes: A new computational procedure, *International Journal of Refrigeration*, 32, 2009, 162-174.

[22] Doretti L., Zilio C., Mancin S., Cavallini A., Condensation flow patterns inside plain and microfin tubes: A review, *International Journal of Refrigeration,* 36, 2013, 567-587.

[23] Olivier J.A., Liebenberg L., Thome J.R., Meyer J.P., Heat transfer, pressure drop, and flow pattern recognition during condensation inside smooth, helical micro-fin, and herringbone tubes, *International Journal of Refrigeration*, 30, 2007, 609-623.

[24] Thome J.R., El Hajal J., Cavallini A., Condensation in horizontal tubes, part 2: new heat transfer model based on flow regimes, *International Journal of Heat and Mass Transfer*, 46, 2003, 3365-3387.

[25] Colombo L., Lucchini A. , Muzzio A., Flow patterns, heat transfer and pressure drop for evaporation and condensation of R134A in microfin tubes, *International Journal of Refrigeration*, 35, 2012, 2150-2165.

[26] Zhang X., Zhang X., Chen Y., Yuan X., Heat transfer characteristics for evaporation of R417A flowing inside horizontal smooth and internally grooved tubes. *Energy Conversion and Management*, 49, 2003, 1731–1739.

[27] Li Z., Lu J., Tang G., Liu Q., Wu Y., Effects of Rib Geometries and Property Variations on Heat Transfer to Supercritical Water in Internally Ribbed Tubes. *Applied Thermal Engineering*, 2015, doi: 10.1016/j.applthermaleng.2014.12.067.

[28] Grauso S., Mastrullo R., Mauro A.W., Thome J.R., Vanoli G.P., Flow pattern map, heat transfer and pressure drops during evaporation of R-1234ze(E) and R134a in a horizontal, circular smooth tube: Experiments and assessment of predictive methods. *International Journal of Refrigeration*, 36 ,2013, 478-491.

[29] Del Col D., Bortolato M., Azzolin M., Bortolin S., Condensation heat transfer and two-phase frictional pressure drop in a single minichannel with R1234ze(E) and other refrigerants. *International Journal of Refrigeration*, 50, 2015, 87–103.

[30] Mendoza-Miranda J.M., Ramirez-Minguela J.J., Munoz-Carpio V.D., Navarro-Esbri J., Development and validation of a micro-fin tubes evaporator model using R134a and R1234yf as working fluids, *International Journal of Refrigeration*, 27(1) , 2015, 32-43.
[31] Shklover G.G., Mil'man O.O., Baskov V.S., Ankudinov G.A., Heat transfer in condensation of steam on finely-finned horizontal tubes, *Heat Transfer – Sov. Res.*, 13 (2), 1981, 108–114
[32] Ji W., Zhao C., Zhang D., Li Z., He Y., Tao W. Condensation of R134a outside single horizontal titanium, cupronickel (B10 and B30), stainless steel and copper tubes, *International Journal of Heat and Mass Transfer*, 77 , 2014, 194–201
[33] Sajjan S.K., Kumar Ravi, Gupta Akhilesh, Experimental investigation of vapor condensation of iso-butane over single horizontal plain tube under different vapor pressures, *Applied Thermal Engineering* , 76, 2015, 435e440
[34] Yun R., Heo J., Kim Y., Film condensation heat transfer characteristics of R134a on horizontal stainless steel integral-fin tubes at low heat transfer rate, *International journal of refrigeration* 32, 2009, 865–873,
[35] Zhao Z., Li Y., Wang L., Zhu K., Xie F., Experimental study on film condensation of superheated vapour on a horizontal tube, *Experimental Thermal and Fluid Science* 61, 2015, 153–162
[36] Ribatski G., Jacobi A., Falling-film evaporation on horizontal tubes—a critical review, *International Journal of Refrigeration* 28 ,2005, 635–653.
[37] Kukulka D.J., Smith R., Fuller K., Development and evaluation of enhanced heat transfer tubes, *Applied Thermal Engineering*, 31(13) , 2011a, 2141–2145.
[38] Kukulka D. J., Smith R., Zaepfel J., Development and evaluation of vipertex enhanced heat transfer tubes for use in fouling conditions, *Theoretical Foundations of Chemical Engineering*, 25(6), 2012, 627-633.
[39] Kukulka D.J., Smith R., Thermal-hydraulic performance of Vipertex 1EHT enhanced heat transfer tubes. *Applied Thermal Engineering*, 61(1), 2013, 60-66.
[40] Kukulka D.J., Smith R., Heat transfer evaluation of an enhanced heat transfer tube bundle. Energy, 75, 2014, 97-103.
[41] Kukulka D. J., Smith R., Li W., Comparison of tubeside condensation and evaporation characteristics of smooth and enhanced heat transfer 1EHT tubes, *Applied Thermal Engineering*, 2015, DOI10.1016/j.applthermaleng.2015.01.066
[42] Guo S., Wu Z., Li W., Kukulka D., Sundén B., Zhou X., Simon T. Condensation and evaporation heat transfer characteristics in horizontal smooth, herringbone and enhanced surface EHT tubes , *International Journal of Heat and Mass Transfer* 85, 2015, 281–291
[43] Wu Z., Wu Y., Sundén B., Li W., Convective Vaporization in Micro-Fin Tubes of Different Geometries, *Experimental Thermal and Fluid Science*, 44, 2013, 398-408.
[44] Wu Z., Sundén B., Wang L, and Li W., Convective condensation inside horizontal smooth and microfin tubes, *Journal of Heat Transfer*, 136(5), 2014, 051504-051504-11, doi 10.1115/1.4026370.
[45] Li G. Q., Wu Z., Li W., Wang Z. K., Wang X., Li H. X., Yao S. C., Experimental Investigation of Condensation in Micro-Fin Tubes of Different Geometries, *Experimental Thermal and Fluid Science*, 37, 2012, 19-28.

BOUNDARY CONDITION INVESTIGATION FOR CAVITY FLOW NATURAL CONVECTION

Mahdavi M., Ghodsinezhad H., Sharifpur M.* and Meyer J.P.
*Author for correspondence
Department of Mechanical and Aeronautical Engineering,
University of Pretoria,
Pretoria, 0002,
South Africa,
E-mail: Mohsen.Sharifpur@up.ac.za

ABSTRACT

Natural Convection in confined enclosures has been one of the research interests because of the application in a wide range of engineering areas such as power plants, cooling systems, solar collectors and energy storage technologies. It seems that a rectangular cavity exhibits a simple geometry for experimental purposes; however, the existence of low range of velocity and heat transfer in natural convection remains the measurement challenges. Also, complete modeling (the cavity and heat exchangers) is so complicated from the aspects of the flow regime and heat transfer, especially with the presence of turbulence. In this research, both experimental and numerical models of water natural convection inside a cavity are presented. The experiment aims to keep the hot and cold walls in constant temperature. The numerical simulation consists of 3D full model of the experimental set-up and a 2D model of the cavity as well. A comparison among results proves that the existence of a small gradient of temperature in both cold and hot walls is unavoidable.

INTRODUCTION

A large number of researches for cavities are focused on numerical simulations and mostly 2D, and a few experimental works are available [1].

Inaba and Fukuda [2] conducted both experimental and numerical study on laminar convection in a small cavity 15mm×15mm×100mm with water inside at its maximum density at 4 ^{o}C. Two walls were kept at uniform temperature, cold one with a constant temperature bath and the hot one with an electrical heater. They simulated a 2D model for the cavity and showed that the 2D assumption of the cavity can provide proper results in this case due to high horizontal aspect ratio, also stated by Ampofo and Karayiannis [3] for the aspect ratio above 1.8. Braga and Viskanta [4] performed the same experiment in transient laminar flow with similar thermal boundary conditions and water inside. They proposed that the flow is laminar with modified Rayleigh number at the order of 10^8, although Rayleigh number above 10^6 was considered turbulent with air inside the cavity by Markatos and Pericleous [5] and definitely above 10^8 by Kuyper et al. [6]. Aydin and Yesiloz [1] performed numerical and experimental research on natural flow convection in a quadrantal enclosure with water inside in laminar region. The radius and depth were 30mm×60mm, respectively, and geometry was modelled 2D.

Experimental studies with air inside cavity were presented as the following:

NOMENCLATURE

c_p	[J/^{o}K]	specific heat
K	[W/mK]	Thermal conductivity
k	[m^2/s^2]	turbulent kinetic energy
L	[m]	Distance between hot and cold walls
Nu	[-]	Nussult number
P	[N/m^2]	Pressure
Ra	[-]	Rayleigh number
T	[K]	Temperature
x_j	[m]	Cartesian axis directions

Special characters

α	[m^2/s]	Thermal Diffusivity
β	[1/^{o}K]	thermal expansion coefficient
μ	[kg/m.s]	Dynamic viscosity
μ_t	[kg/m.s]	turbulent viscosity
υ	[m^2/s]	Kinematic viscosity
ρ	[kg/m^3]	density
ε	[m^2/s^3]	Turbulence dissipation rate

Subscripts

c-cavity	Cold side of the cavity
h-cavity	Hot side of the cavity

Leong et al. [7] conducted some tests on 127mm side wall cavity with hot plate on top and cold plate on bottom with two separate water streams for heating and cooling. They reported the linear distribution of temperature on side walls. Tian and Karayiannis [8] carried out a benchmark experiment on a rather big cavity, 750mm×750mm×1500mm, in turbulent flow and Rayleigh number above 10^9, with K-type thermocouple and 0.02 accuracy, using cold and hot constant temperature baths for isothermal walls. Salat et al. [9] performed some turbulent natural convection tests inside a large cavity 1m×1m×0.32m on cross section with constant temperature on side walls and adiabatic walls on the top and bottom. In spite of the large size of the cavity, they reported the presence of constant temperature in both walls with using cold and hot heat exchangers in each side.

A large number of numerical studies can be found for natural convective flow inside cavities in literature. Aydin and Yang [10] simulated laminar flow in a 2D square cavity with air inside and suggested that the heat transfer is mostly dominated by conduction in lower Rayleigh number and convection in higher Rayleigh number. Dixit and Babu [11]

showed that a very fine mesh with $y^+<0.3$ is needed for higher Rayleigh number in natural convection.

It has been found out from literature review that most of the experimental work is for air-filled cavities and a few experimentations are available for water inside a cavity. On the other hand, most of numerical simulations in the literature consist of 2D models with Prandtl number 0.71, which is for gas or air. It can be explained that water is able to produce more powerful conductive and convective flow than air inside a cavity, which makes it difficult to reach uniform distribution of temperature on the walls for experiment purposes. In this study, it has been observed that isothermal walls can be easily achieved with the presence of air. While the experimentations with water have revealed some non-uniformities on the walls temperatures. Hence, both experimental and numerical study of natural convection flow with water inside a cavity were performed in this research. On the knowledge of authors, this is the first report which takes into account the full 3D model of whole set-up for a cavity and both water circulations in heating and cooling sections.

EXPERIMENTAL SETUP AND PROCEDURES

The size of the cavity used in this study is 96mm×120mm for cold and hot walls and 102mm the space between those walls. The entire schematic of the test section is shown in Figure 1. The hot and cold wall sides of the cavity are heated and cooled by two shell and tube heat exchangers with counter flow inside. All the materials here were fabricated from copper, including 8mm copper plates in each side of cavity. The dimensions of the shell part of heat exchanger are 96mm×120mm×18mm. To improve the heat transfer and uniformity of the temperature inside the heat exchanger, the mass flow from and to heat exchanger is split between shell and tube parts. Also, three fin-plate made of copper with 2mm thickness were installed inside heat exchanger as buffers to extend heat transfer surfaces. Two constant hot and cold baths are employed to keep the required amount of water mass flow rate inside the heat exchanger in certain temperature. The diameter of the tube was chosen 10.7mm ID and 1mm wall thickness. The hydraulic diameter of the shell part was calculated similar to tube diameter to achieve the best distribution of mass and heat transfer inside heat exchangers. To reduce the amount of heat losses from all apparatus shown in figure 1a to ambient, 12mm of insulation layer made of polystyrene were attached to the visible surfaces. Afterward, it was put in a big box made of wood and the void regions inside the box were filled with the same insulator. Three T-type thermocouples with accuracy ±0.2 and 1mm in diameter were placed in each side of the cavity inside the copper layer to monitor the temperature at the top, middle and bottom of the wall (Figure 1b). Two thermocouples were put inside tube flow in hot and cold sides to measure the inlet and outlet temperature.

The measured data reveals that temperature drop is less than 1 °C in most of the tests. Therefore, it is crucial to utilize high accurate temperature measurement to calculate the rate of heat transfer properly from $\dot{m} c_p \Delta (T_{out} - T_{in})$.

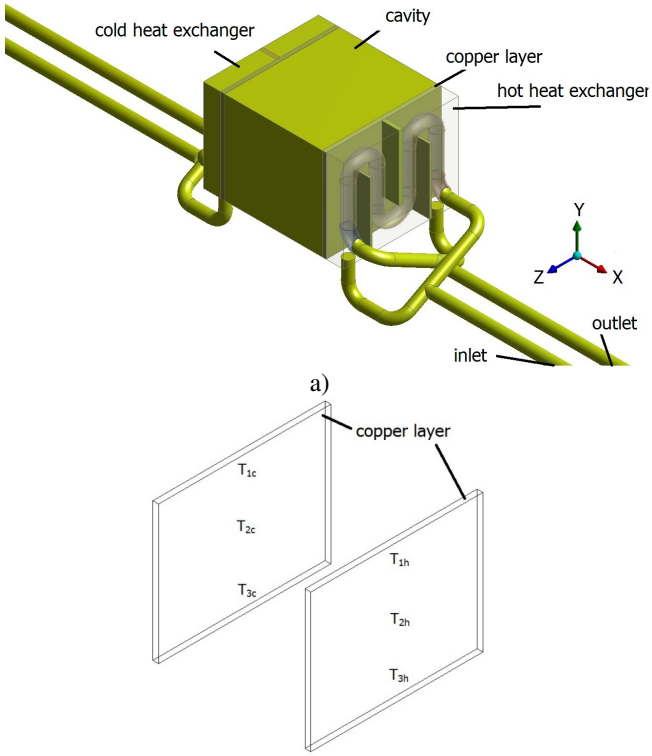

Figure 1. Schematic of test section

GOVERNING EQUATIONS AND NUMERICAL APPROACH

With the calculation of Reynolds number in heat exchangers and Rayleigh number defined as the following, three separate types of flow regimes are recognized in the experiment: turbulent flow in hot heat exchanger with Reynolds number above 3500, laminar flow in cold heat exchanger with Reynolds number less than 2000 and turbulent natural convection flow in cavity with Rayleigh number above 10^8.

$$Ra = \frac{g\beta L^3 (T_{h-cavity} - T_{c-cavity})}{\alpha \nu} \quad (1)$$

Where L is the space between hot temperature $T_{h-cavity}$ and cold temperature $T_{c-cavity}$ in the cavity. All the thermo-physical properties of Rayleigh number are evaluated based on the average temperature $(T_{h-cavity} + T_{c-cavity})/2$. The amount of Rayleigh number in this cavity happens more than 1.5×10^8 which can be considered turbulent.

A short form of continuity, momentum and energy equations are formulated as:

$$\frac{\partial \overline{u}_i}{\partial x_i} = 0 \quad (2)$$

$$\rho u_j \frac{\partial \overline{u}_i}{\partial x_j} = -\frac{\partial \overline{P}}{\partial x_i} + \frac{\partial}{\partial x_j}\left[\mu \frac{\partial \overline{u}_i}{\partial x_j} - \rho \overline{u_i' u_j'}\right] + g_i \beta (T - T_{c-cavity}) \quad (3)$$

$$\rho \overline{u}_j \frac{\partial \overline{T}}{\partial x_j} = \frac{1}{c_P}\frac{\partial}{\partial x_j}\left[\mathrm{K}\frac{\partial \overline{T}}{\partial x_j} - \rho c_P \overline{T' u_j'}\right] \quad (4)$$

The transport equations for turbulent kinetic energy *k* and dissipation rate ε and also viscosity is shortly presented as the following:

$$\frac{\partial}{\partial x_i}(\rho k u_i) = \frac{\partial}{\partial x_i}\left(\left[\mu + \frac{\mu_t}{\sigma_k}\right]\frac{\partial k}{\partial x_i}\right) + G_k + G_b - \rho\varepsilon - Y_M + S_k \quad (5)$$

$$\frac{\partial}{\partial x_i}(\rho \varepsilon u_i) = \frac{\partial}{\partial x_i}\left(\left[\mu + \frac{\mu_t}{\sigma_\varepsilon}\right]\frac{\partial \varepsilon}{\partial x_i}\right) + \rho C_1 S\varepsilon - \rho C_2 \frac{\varepsilon^2}{k + \sqrt{\nu\varepsilon}} + C_{1\varepsilon}\frac{\varepsilon}{k} C_{3\varepsilon} G_b + S_\varepsilon \quad (6)$$

$$\mu_t = \rho C_\mu \frac{k^2}{\varepsilon} \quad (7)$$

It is noted that equations 1 to 4 are only valid for natural convection if $\beta\Delta T \ll 0.1$, which is the necessity for the validity of Boussinesq approximation.

NUMERICAL SOLUTION, GRID GENERATION AND BOUNDARY CONDITIONS

Coupled solver in steady state situation via CFD code ANSYS-FLUENT 15 were employed to solve the time averaged equations of Navier Stockes or Reynolds averaged equations for turbulent flow. In spite of segregated solvers such as SIMPLE, Both momentum and pressure based continuity equations are iteratively solved at the same time in Coupled solver. Because of high complexity of flow regimes in this study, it is essential to use this solution method. The maximum difference between hot and cold walls temperature in the cavity is less than 30°C ($\beta\Delta T \ll 0.1$), thus density in y-direction is approximated only in the cavity by boussinesq function. Second order upwind interpolation scheme were used to discretize momentum convective and diffusion terms, turbulent kinetic energy, turbulent dissipation rate and energy equation terms. Due to noticeable impacts of buoyancy-driven force in the cavity, Body force weighted scheme were chosen to interpolate pressure in the equations.

Both structured and unstructured meshes are required for this kind of geometry; unstructured mesh for heat exchangers and structured one for cavity and copper layers. Also, boundary layer meshes are added in the heat exchangers due to small size of the tube and existence of turbulent flow inside hot section. . Realizable *k-ε* model was operated with enhanced wall function as wall treatment in shell and tubes. The initial results exhibited the amount of y^+ at the vicinity of the all walls less than 5, which is acceptable amount for this method. On the other hand, the natural convection simulations inside the cavity proved that the mesh must be fine enough ($y^+ < 0.5$) at the vicinity of the walls to capture the entire influences of small boundary layer due to natural convection. As a result, the closest node to the shell and tube walls was chosen 0.4 mm and 0.3mm for cavity. Three kinds of flow regimes exist in the model, turbulent force convection, laminar convection and turbulent natural convective flow. Therefore, it can be expected to require a large number of iterations to reach heat transfer balance in the cavity, which is the most important criteria for convergence. Various number of meshes were tried to find the optimum and best grid for each section in the model concerning grid study (up to 2 million nodes in total). The criteria for comparison among different grids were chosen heat flux in walls, temperature and velocity profile at the centre line of the cavity. Eventually, the proper mesh was chosen 224065 unstructured nodes for each heat exchanger and 216000 structured nodes for cavity, and 694279 nodes for entire model. Generated mesh for the tube part of heat exchanger and cavity is shown in figure 2a and 2b, respectively. The working fluid in all the parts is water with thermo-physical properties as a function of temperature. Uniform velocity and temperature are assigned for the inlet of both hot and cold heat exchangers and pressure outlet is chosen for exits of the tubes.

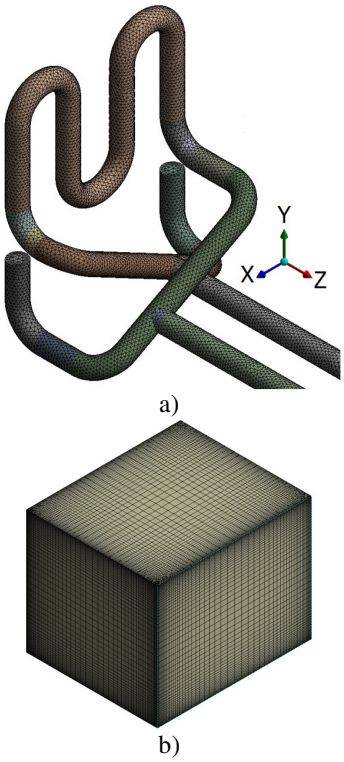

a)

b)

Figure 2. The generated mesh for a) tube of heat exchanger (unstructured) b) cavity (structured)

RESULTS AND DISCUSSION

It was observed that presence of temperature gradient in hot and cold wall of the cavity is unavoidable. Also, numerical results exhibited the same pattern in the walls. The maximum

temperature difference in each wall is between 2 to 3 degrees for both measured and estimated temperature. Nusselt number is calculated from the following with thermo-physical properties based on hot and cold wall average temperature:

$$\overline{Nu} = \frac{q'' L}{K(T_{h-cavity} - T_{c-cavity})} \quad (8)$$

where q'', $T_{h-cavity}$ and $T_{c-cavity}$ are aerial average of heat flux, average temperature on hot and cold walls of the cavity, respectively. In spite of high Rayleigh number in all the tests, there are still some doubts to assume the entire flow inside the cavity as turbulent. Because each vertical wall behaves as a vertical plate and turbulence occurs only in a small area in downstream. However, CFD analyses have revealed that both the assumptions of laminar and turbulent flow inside this cavity provide the same value for average Nusselt number. Therefore, turbulence model is chosen for this study.

Figure 3 and 4 show the average Nusselt number and temperature distribution at the centre-line of the cavity provided by experiment, full 3D model with heat exchangers, cavity as 3D model and only cavity as 2D model. Average temperature of the cold and hot walls from experimentation is assigned as uniform temperature boundary conditions for 2D and 3D models of cavity itself. As can be seen, there is a full agreement between simulations and measurements. The difference between Nu number estimated by models with uniform wall temperature and full model is less than 5%. Both 2D and 3D models predicted the same amount of distribution of temperature in horizontal centreline of cavity. Although, small discrepancy of temperature profile in vertical centreline between full model and the other models is observed in Figure 4a. Since the temperature in downstream of hot wall is higher than wall average temperature (this average was chosen as boundary condition for two other models), the full model and experiment have provided higher temperature in top half of cavity comparing to other models. The similar analysis can be made for bottom half, but in an opposite way.

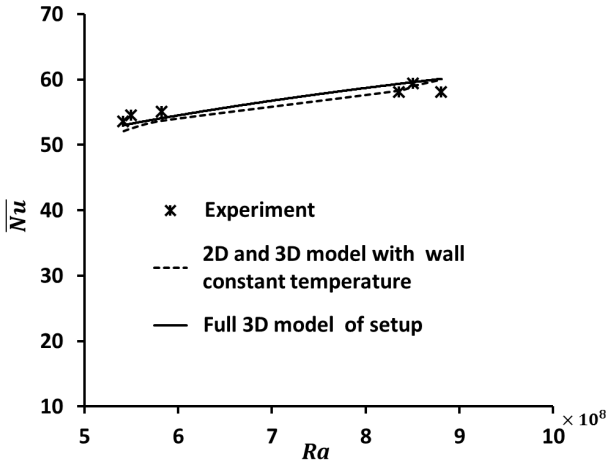

Figure 3. Average Nusselt number from measurements and simulation results

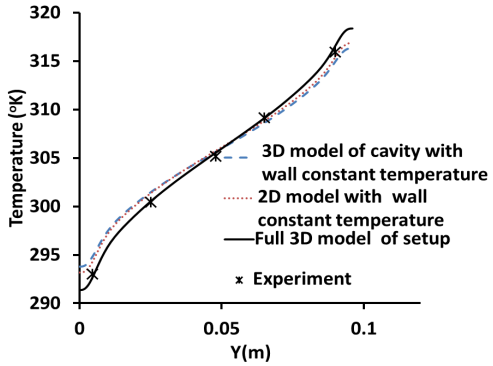

a)

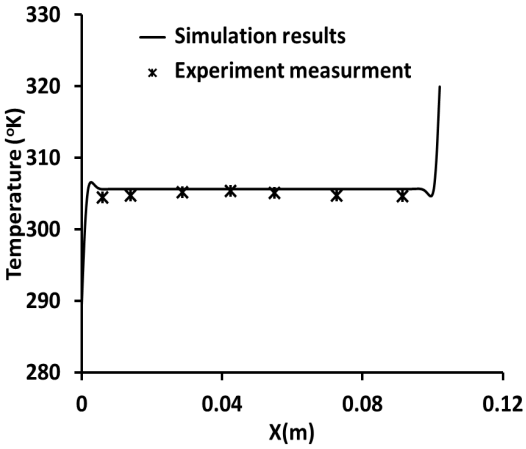

b)

Figure 4. Temperature distribution at the a) vertical centreline between top and bottom insulated walls b) horizontal centreline of the cavity from cold to hot walls at Ra=8.81×10^8

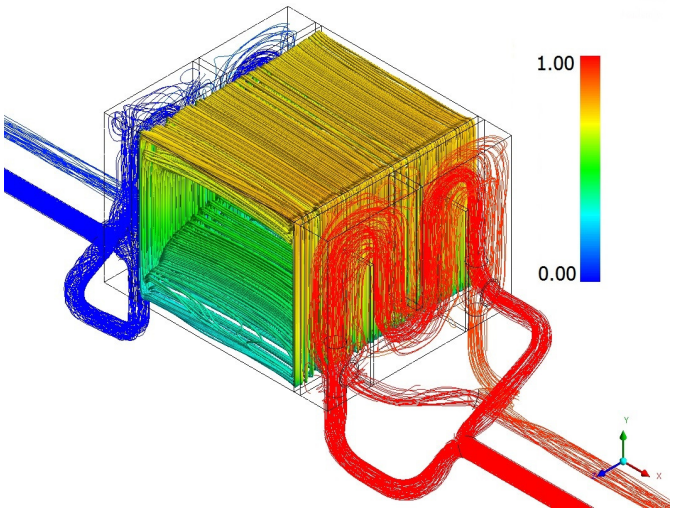

Figure 5. Streamlines of flow field inside the cavity and heat exchangers coloured by non-dimensional temperature

In spite of almost uniform distribution of temperature inside both heat exchangers, the temperature on the walls of cavity differs from the force flow next to it, as can be seen in Figure 5

with non-dimensional temperature defined as: $\frac{T-T_c}{T_h-T_c}$. It comes from the fact that removal of heat transfer at the vicinity of the walls inside the cavity changes in y-direction, which brings up a boundary layer with high gradient of temperature in the side of heat exchangers attached to the walls of cavity.

Flow stream function for 2D case with constant temperature on the walls is presented in figure 6. To compare the discrepancy with 3D models, Figure 7 shows the streamlines of half of the cavity simulated by full model and the cavity itself, coloured by non-dimensional magnitude of velocity defined as $\frac{U}{\sqrt{g\beta L\Delta T}}$ at Ra=7.86×10^8.

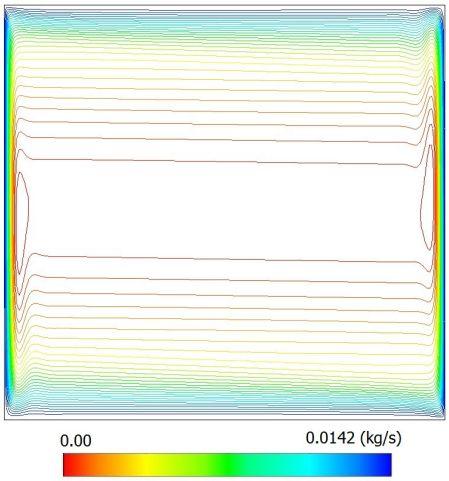

Figure 6. Stream function predicted by 2D model with constant temperature on the walls.

The flow structure is totally different in 3D cavity with constant temperature on the walls than full model of set-up. Also, the magnitude of velocity seems more at the vicinity of the walls in the case of constant wall temperature. Two parabolic streamlines are seen in full model simulations. As can be expected, 2D model is not able to capture the parabolic behaviour of the flow stream close to the corners and insulated walls. Streamlines are more uniform in 3D cavity in Figure 7a and the similarity is visible with 2D model streamlines.

The main difference among simulations can be more visible with the changes of velocity profile in the boundary layer close to the hot wall. Full model of the setup assumes perfect insulation for adiabatic walls and ignores the local loses of heat transfer caused by ambient temperature. However, the effects of these loses are not comparable to the total rate of heat transfer. Furthermore, some changes in the profile of velocity induced by buoyancy force are expected. This is one of the drawbacks of the full model comparing to the real geometry. Figure 8 presents these discrepancies with the other simulations with constant wall temperature. The profiles for the 2D and 3D models with constant temperature are similar and more than the one predicted by full model. It proves that water inside the cavity with aspect ratio about 1 can be treated as two-dimensional flow with high accuracy.

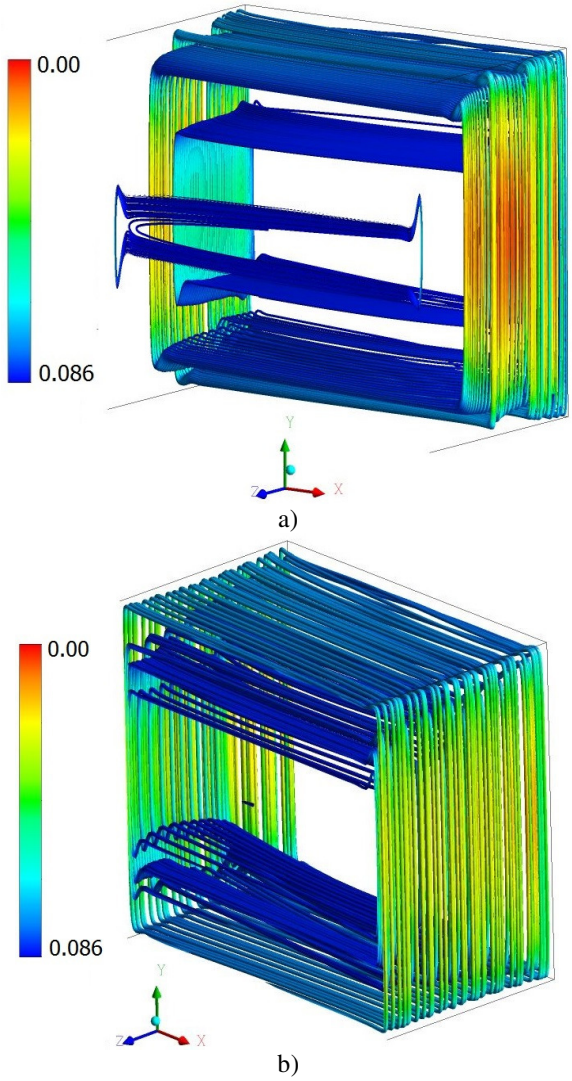

Figure 7. Streamlines predicted by a) 3D model of cavity itself with constant temperature on the hot and cold walls b) full model of the set-up, both coloured with magnitude of velocity

CONCLUSION

The effects of uniform temperature boundary condition on the hot and cold walls of a cavity were compared with full model of the set-up and experimental data. The cavity along with both vertical heat exchangers on the sides was simulated in this study as the full model and the predictions were in perfect agreement with experimentations. Due to complexity of the whole set-up and large number of computational cells, it was essential to present a simpler substitution. Hence, 2D and 3D models of cavity itself were simulated with uniform temperature coming from average temperature of the hot and cold walls of the experimental tests. In spite of difference between velocity profiles from full model with these simpler ones in boundary layer close to the wall, the predictions for Nusselt number has revealed less than 5% error with measurements and full model results. Eventually, it can be

concluded that a cavity with aspect ratio close to unity with water inside and small gradient of temperature at the side walls can be simulated as a simple 2D geometry with uniform temperature instead with error less than 5% comparing to full model of the setup. It is also noted that it is still crucial to employ full model if the observation of flow field inside a cavity is the case, rather than only the heat transfer characteristics of the cavity.

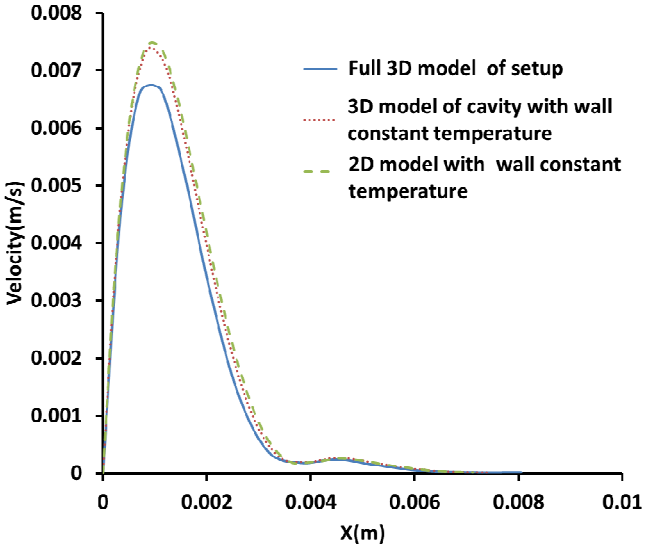

Figure 8. Profile of the velocity in boundary layer close to the hot wall of the centreline of the cavity at Ra=7.86×10^8

REFERENCES

[1] Orhan A, Gurkan Y. Natural Convection in a Quadrantal Cavity Heated and Cooled on Adjacent Walls. *Journal of Heat Transfer*, v. Vol. 133, 2011, pp. 052501-1-7

[2] Inaba, H.; Fukuda, T. Natural convection in an inclined square cavity in regions of density inversion of water. *Journal of Fluid Mechanics*, Vol. 142, 1984, pp. 363- 381

[3] Ampofo, F., Karayiannis, T.G. Experimental benchmark data for turbulent natural convection in an air filled square cavity. *International Journal of Heat and Mass Transfer*, v. 46, 2003, pp. 3551–3572

[4] Braga, S. L., Viskanta, R. Transient natural convection of water near its density extremum in a rectangular cavity. *International journal of heat and mass transfer*, v. 35, 1992, pp. 861-875

[5] Markatos, N. C., Pericleous, K. A. Laminar and turbulent natural convection in an enclosed cavity. *International Journal Of Heat And Mass Transfer*, v. 27, 1984, pp. 755-772

[6] Kuyper, R. A., Van Der Meer, Th. H., Hoogendoom, C. J., Henkes, R.A.W.M. Numerical study of laminar and turbulent natural convection in an inclined square cavity. *International Journal of Heat and Mass Transfer*, v. 36, 1993, p. 2899–2911

[7] Leong, W. H., Hollands, K. G. T., Brunger, A. P. Experimental Nusselt numbers for a cubical cavity benchmark problem in natural convection. *International Journal of Heat and Mass Transfer,* v. 42, 1999, p. 1979-1989

[8] Tian, Y.S., Karayiannis, T.G. Low turbulence natural convection in an air filled square cavity Part I: the thermal and fluid flow fields. *International Journal of Heat and Mass Transfer*, v. 43, 2000, p. 849-866

[9] Salat, J., Xin, S., Joubert, P., Sergent, A., Penot, F., Le. Quere. Experimental and numerical investigation of turbulent natural convection in a large air-filled cavity. *International Journal of Heat and Fluid Flow*, v. 25, 2004, p. 824–832

[10] Aydin, O. Yang, W.J. Natural convection in enclosures with localized heating from below and symmetrical cooling from sides. *International Journal of Numerical Methods for Heat & Fluid Flow,* v. 10, 2000, p. 518 - 529,.

[11] Dixit, H.N. Babu, V. Simulation of high Rayleigh number natural convection in a square cavity using the lattice Boltzmann method. *International Journal of Heat and Mass Transfer,* v. 49, 2006, p. 727–739

Entropy Generation And Convective Heat Transfer Of Graphene Nanoplatelets Nanofluid For Laminar Forced Convection Flow

Mohammad Mehrali[a*], Emad Sadeghinezhad[b*], Sara Tahan Latibari[a], Mehdi Mehrali[a], Hendrik Simon Cornelis Metselaar[a]
*Author for correspondence
[a] Department of Mechanical Engineering and Advanced Material Research Centre, University of Malaya, 50603 Kuala Lumpur, Malaysia
[b] Department of Mechanical Engineering, University of Malaya, 50603 Kuala Lumpur, Malaysia Department of Mechanical and Aeronautical Engineering,
E-mail: mohamad.mehrali@siswa.um.edu.my

ABSTRACT

The results are reported of an investigation of the heat transfer characteristics and entropy generation for a graphene nanoplatelets (GNP) nanofluid with specific surface area of 750 m^2/g under laminar forced convection conditions inside a circular stainless steel tube subjected to constant wall heat flux. The analysis considers constant velocity flow and a concentration range from 0.025 wt% to 0.1 wt%. The impact of the dispersed nanoparticles concentration on thermal properties, convective heat transfer coefficient, thermal performance factor and entropy generation is investigated. An enhancement in thermal conductivity for GNP of between 12% and 28% is observed relative to the case without nanoparticles. The convective heat transfer coefficient for the GNP nanofluid is found to be up to 15% higher than for the base fluid. The heat transfer rate and thermal performance for 0.1 wt% of GNP nanofluid is found to increase by a factor of up to 1.15. For constant velocity flow, frictional entropy generation increases and thermal entropy generation decreases with increasing nanoparticle concentration. But, the total entropy generation tends to decrease when nanoparticles are added at constant velocity and to decrease when velocity rises. Finally, it is demonstrated that a GNP nanofluid with a concentration between 0.075 wt% and 0.1 wt% is more energy efficient than for other concentrations. It appears that GNP nanofluids can function as working fluids in heat transfer applications and provide good alternatives to conventional working fluids in the thermal fluid systems.

INTRODUCTION

Conventional heat transfer fluids have naturally low thermal conductivities, significantly limiting the heat exchange efficiency of heat exchangers in which they are used [1]. As materials modifications, use of extended surfaces, process parameter alterations and redesigning heat exchange equipment have already been exploited extensively to increase heat transfer rates, many research activities have now focused on enhancing the heat transfer fluid. Improving the thermal transport properties of fluids by adding thermally conductive solid particles has become a prominent research avenue [2]. A nanofluid is a suspension of nanoparticles in a base fluid, and nanofluids are considered promising heat exchanger fluids for enhancing heat transfer due to their high thermal conductivities. Presently, discrepancies exist in the literature regarding nanofluid thermal conductivity data, and the heat transfer enhancement mechanisms are not yet fully understood [3]. The heat transfer enhancement provided by nanofluids has been attributed to many mechanisms, including the following: 1) particle agglomeration, 2) nanoparticle concentrations, 3) Brownian motion, 4) thermophoresis, 5) nanoparticle size, 6) particle shape/specific surface area, 7) liquid layering on the nanoparticle-liquid interface, 8) working temperature, and 9) reduction in thermal boundary layer thickness [4]. Most research has focused on how various parameters affect thermal properties, rather than on the heat transfer process. It is generally more beneficial to add nanoparticles, when the base working fluid of a system has low thermal conductivity. The selection of the base fluid is primarily dependent on the heat transfer application specifications. One concern with the use of nanoparticles is that, although their dimensions are several nanometers, larger particles can lead to damage and corrosion difficulties for equipment such as pipelines and flow channels due to their high momentum and energy [5].

The convective heat transfer coefficient has been investigated experimentally in a flow loop at various flow rates and various nanoparticles sizes, concentrations and types (Al_2O_3 , TiO_2, MgO, Cu, CuO, SiC, Ag, CNT) [6]. A number of experimental investigations have been reported on nanofluid flow in a tube. Researchers have experimentally observed for laminar flow heat transfer enhancements of up to 106% through the use of nanofluids [7, 8]. Ding, Alias, Wen and Williams [9] found the relative enhancement of local heat transfer coefficient reached 350% for nanofluids with 0.5 wt.% carbon nanotube (CNT). Other researchers have reported lower local heat transfer coefficient enhancements for CNT nanofluids at higher concentrations [10, 11]. Additionally, some researchers have reported that the heat transfer for nanofluids follows classical correlations for single phase fluids [12].

The performance of a thermal system can be assessed in part by determining the heat transfer characteristic of heat transfer fluid and the entropy generation. It has been shown that augmentation of convective heat transfer flow does not ensure improvement of thermodynamic efficiency due to irreversibilities [13], which can be measured by total entropy

generation of when using nanofluids. Entropy generation analysis has been used to determine the more efficient of numerous thermal systems, where the entropy generation is caused by irreversibilities associated with such processes as chemical reaction, mixing, friction, heat transfer across finite temperature differences [13]. Bejan [14] has determined the entropy generation for forced convection for various geometries including circular tubes, boundary layers over a flat plate, and cross flow over a single cylinder.

Recently, significant research has been conducted on the use of carbon based nanostructure materials (i.e. graphene) to prepare nanofluids [15-17]. Graphene is a single-atom-thick sheet of hexagonally arrayed sp^2-bonded carbon atoms and has received considerable attention since it was discovered by Novoselov, Geim, Morozov, Jiang, Zhang, Dubonos, Grigorieva and Firsov [18]. Graphene has attracted attention due to its advantageous thermal, mechanical, electrical, optical and other relevant characteristics. Research on graphene has focused on its characteristics, often using various spectroscopic and microscopic experimental techniques [19]. Based on the literature, however, data are lacking on flows of water-based graphene nanoplatelets (GNP) nanofluids in horizontal tube heat exchangers under laminar flow conditions [20]. Additionally, investigations have not been reported on the entropy generation of GNP nanofluids under laminar convective heat transfer in circular tubes subjected to a constant wall heat flux. Thus, it is intention of this research to bridge this gap and improve understanding of heat transfer and entropy generation for GNP nanofluids for such conditions.

In this article, GNP nanoparticles with a specific surface area of 750 m^2/g are dispersed in water to prepare nanofluids with concentrations up to 0.1 wt%. Then, thermophysical properties of the nanofluids, including thermal conductivity and viscosity, are measured, and flow and heat transfer characteristics of the nanofluids are evaluated, including heat transfer coefficient (h), pressure drop, entropy generation, and thermal performance factor. The variation of the convective heat transfer coefficient is investigated under a heat flux of 3,500 W/m^2 and an inlet temperature of 30°C at various concentrations of GNP nanofluid up to 0.1 wt% for bulk velocities ranging from 0.05 to 0.4 m/s (for which the Reynolds number Re varies from 290 to 2,300).

A shift towards the modular integration of power electronics, resulting in increased power and loss densities [1], have necessitated the development of more effective cooling methods to reduce peak operating temperatures in such applications [2,3]. Due to low thermal conductivities associated with the outer material layers of these integrated power electronic modules [2,3], surface cooling on its own is no longer sufficient as the materials themselves act as major thermal barriers [4]. Internal heat transfer augmentation of these solid-state heat-generating volumes via the creation of low thermal resistance paths to surface regions has become crucial. Through this, restrictions placed upon future development by thermal issues may be made less critical due to the fact that components can be operated at higher power densities and at relatively lower peak temperatures.

Solid state conductive cooling, being a passive cooling scheme and not being dependent on other support systems, exhibits reliability and volumetric advantages. Even though conductive heat transfer may be orders lower than heat transfer associated with convection or evaporation, its reliability aspect justifies in-depth investigations into cooling methods using this heat transfer mode.

NOMENCLATURE

c_p	Specific heat capacity at constant pressure, J/kg K
d	Tube diameter, m
DW	Distilled water
$\dot{E}_{gen}$	Entropy generation rate, W/K
f	Friction factor
h	Convective heat transfer coefficient
I	Electrical current, A
k	Thermal conductivity, W/m.K
l	Tube length, m
GNP	Graphene nanoplatelets
$\dot{m}$	Mass flow rate, kg/s
Nu	Nusselt number
P	Pressure, Pa
q″	Heat flux, W/m^2
Re	Reynolds number
T	Temperature, K
UV-vis	UV–vis spectrophotograph
V	Voltage
v	Mean velocity, m/s
x	Axial distance

Greek symbols

μ	Viscosity, Pa.s
ρ	Density, kg/m^3
η	Performance index

Subscripts

avg	average
b	bulk
bf	base fluid
fl	Frictional
i	inner
in	inlet
m	mean
nf	nanofluid
np	nanoparticle
o	outer
out	outlet
Th	thermal
w	wall

EXPERIMENTAL APPROACH AND METHODS

Materials and nanofluids preparation

GNP nanoparticles (Grade C, specific surface area of 750 m^2/g, from XG Sciences, Inc., Lansing, MI, USA) and distilled water are used for the preparation of nanofluids. GNP

nanoparticle diameters of 2 μm and thickness 2 nm are used. Based on our previous work [16], the nanofluid samples are prepared by dispersing GNP nanoparticle in distilled water using a high-powered ultrasonication probe (Sonics Vibra-Cell, VCX 750, from Sonics & Materials, Inc., USA) that has a 750-W output power and a 20-kHz frequency power supply. The nanofluid concentrations examined are 0.025, 0.05, 0.075, and 0.1 wt%.

Experimental set up and procedure for heat

The heat transfer coefficients of GNP nanofluids are measured in horizontal stainless steel tubes with constant heat flux on the outer wall surface. A schematic diagram of the experimental set up is shown in Figure 1. It consists of a flow loop, a heating unit, a cooling unit, measuring instruments, and a jacketed tank. The flow loop includes a pump, a flow meter, a differential pressure transmitter, a nanofluid tank, bypass loop and a test section.

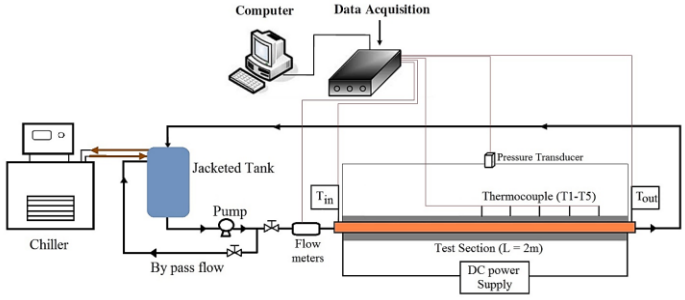

Figure 1 Experimental setup to measure heat transfer coefficient of nanofluids

A straight stainless steel tube of 2000 mm length, 4.5 mm inner diameter, and 6.5 mm outer diameter is used as the test section. The aspect ratio of $L \approx 0.05ReD$ (L = 596 mm) at the entrance of the test section is used to ensure the flow is hydrodynamically developed, and the 1404 mm of test section is heated directly by a DC power supply (N8738A, 3300W, from Agilent Technologies). Five type K thermocouples (self-adhering thermocouple, SA1XL-K-72, of Omega, with $\pm 0.1^{\circ}C$ accuracy) are fixed at the outer surface of the tube at distances from entry of 830 mm (TS1), 1064 mm (TS2), 1298 mm (TS3), 1532 mm (TS4), 1766 mm (TS5) to measure the tube wall temperature. To measure the inlet and outlet bulk fluid temperatures of the test section, two K-type thermocouple (Customized, from Omega, with $\pm 0.1^{\circ}C$ accuracy) are used. All thermocouples are calibrated prior to the experiments. The thermocouples are connected to the Graphtec (midi logger gl220) for the continuous monitoring and recording of the temperature data. To minimize the heat loss to the surroundings, a thick ceramic fiber cloth and calcium silicate bar are installed around the test section.

The nanofluids are pumped from a 2-L capacity jacketed beaker (Pyrex) by a dispensing peristaltic pump (Longer pump BT300-1F, with YZ1515X pump head) then passed through the test section and recycled back to the storage tank to be returned to the required inlet temperature. The nanofluid inside the jacketed tank is cooled by a refrigerated circulating bath (UWK 140/TP2, from Thermo Haake, Karlsruhe, Germany). The flow rate and the pressure loss are measured using flow sensors (FLR1009ST-D, from Omega, with ±3% accuracy) and a differential pressure transmitter (2027P7 Pressure Meter, from Digitron, with ±0.15% accuracy), respectively.

Data processing

The heat transfer behavior of the nanofluids is investigated by evaluating the heat transfer coefficient and the surface temperature. The measurements are performed at bulk velocities ranging from 0.05 to 0.4 m/s (for which the Reynolds number varies from 290 to 2,300). The effect on the convective heat transfer coefficient is described for a heat flux of 3,500 W/m^2, an inlet temperature of $30^{\circ}C$ and various concentrations of the GNP nanofluid. With the measured wall temperature of the stainless steel tube, the inlet and outlet temperatures of test section, the heat flux and the flow rate, the local convective heat transfer coefficient at a general axial position on the heating section is calculated as follows [21]:

$$h(x) = \frac{q''}{T_{w,i}(x) - T_b(x)} \quad (1)$$

Also, with a steady state one dimensional energy balance in the tube, the inner wall temperature is calculated based on the measured outer wall temperature, which is defined as:

$$T_{w,i}(x) = T_{w,o} - \frac{q}{2\pi L k_w} \ln \frac{D_i}{D_o} \quad (2)$$

The convective heat transfer coefficient in Equation (1) is usually expressed in the form of the Nusselt number (Nu), as follows:

$$Nu(x) = \frac{h(x)D}{k} \quad (3)$$

The pressure drop is calculated as follows, based on the Hagen–Poiseuille correlation for single-phase flow:

$$\Delta P = \frac{32\mu v L}{d_i^2} \quad (4)$$

The friction factor is defined as:

$$f = \frac{\Delta P}{\left(\frac{L}{D}\right)\left(\frac{\rho v^2}{2}\right)} \quad (5)$$

Properties of nanofluids

A nanofluid is a colloidal suspension of nanosized metallic or nonmetallic particles in a base fluid. The proper utilization of nanofluids depends on their preparation and stability. Nanofluids are considered to be stable if the concentration of the nanoparticles remains constant with time [16, 22]. Sedimentation of the nanofluids is related to stability and is assessed by UV-vis (UV–vis spectrophotograph) and centrifuge methods.

The stability of the aqueous dispersion of GNP nanofluids, as determined by UV–vis, is shown in Figure 2. The absorption value of λ_{max} at 263 nm is plotted against time over 600 hours and shows that the GNP nanofluids are stable, especially at low concentrations (i.e., < 0.1 wt%). The colloidal stability of the GNP nanofluids are seen in Figure 2 to remain relatively

constant, declining over time by 0%, 1%, 3% and 14%, respectively, for concentrations of 0.025, 0.05, 0.075 and 0.1 wt%.

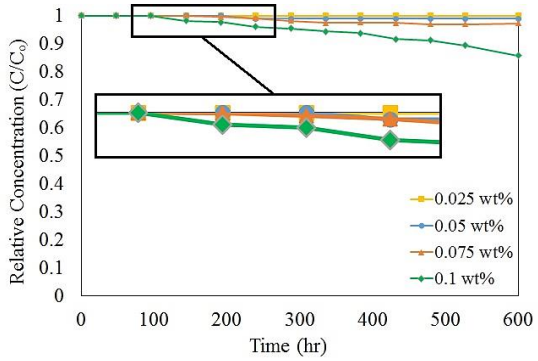

Figure 2 Variation of relative GNP nanoparticle concentration of nanofluids with sediment time.

Determining the sedimentation of nanofluids experimentally is time consuming as it requires a long observation period. Consequently, the dispersions are analyzed here using a dispersion analyzer centrifuge. For this experiment, plastic centrifuge tubes refilled with nanofluids and centrifuged for 5, 10 and 20 min at 6000 rpm. Figure 3 illustrates that, without any surfactants, good dispersion of the GNP nanofluids is achieved, demonstrating that GNP nanofluids are of acceptable stability with a little precipitation for up to 20 min centrifuge time and 6000 rpm. This phenomenon can be explained by the noting that nanoparticles agglomerate, which can occur via sedimentation and particle–particle interactions.

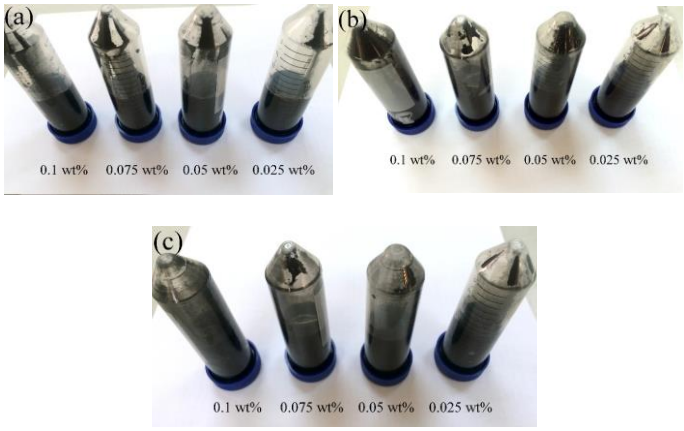

Figure 3 Visual investigation of sedimentation of nanofluids at 6000 rpm for three centrifugation times: (a) 5 min, (b) 10 min, (c) 20 min. Little sedimentation is observed on the bottoms of test tubes for all cases examined.

The thermal conductivity of GNP nanofluids with various concentrations is measured by a KD2 Pro instrument, with an accuracy of ±5%. Figure 4 illustrates the measured thermal conductivity of the GNP nanofluids as a function of temperatures at the considered concentrations. Thermal conductivity enhancement is observed to vary linearly with temperature, and the enhancement of thermal conductivity for GNP nanofluids is between 12% and 28%. The principal mechanism of thermal conductivity enhancement can be explained by the stochastic motion of the nanoparticles. Based on the literature, there is an interfacial resistance between the nanoparticles and base fluid that affects the thermal conductivity of the nanofluids. The suspended nanoparticles in the base fluid experience stochastic bombardment from the ambient liquid molecules through the raising of temperature. This causes irregular motion, called Brownian motion [23]. Brownian motion is related to nanoparticle concentration and fluid temperature [11]. This irregular motion of the nanoparticles is induced from micro mixing or micro convection inside the base fluid. For these reasons, the energy exchange between the base fluid and the nanoparticles is enhanced and the thermal conductivity is enhanced [23].

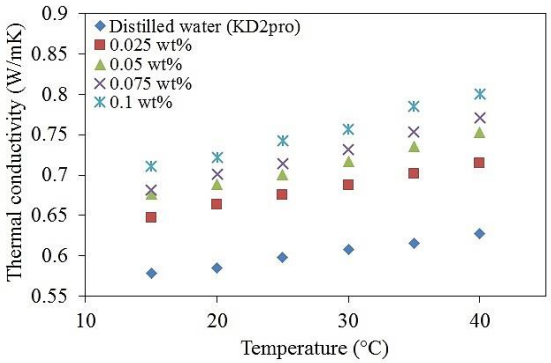

Figure 4 Variation of thermal conductivity with temperature for several GNP concentrations.

Nanofluid viscosity is an important property for applications of nanofluids in thermal systems including cooling systems or heat exchangers. The viscosity of the GNP nanofluids at various concentrations is measured with an Anton Paar rheometer (Physica MCR 301, from Anton Paar GmbH, Graz, Austria) with a 1% error rate at varying working temperatures (see Figure 5). The viscosity of GNP nanofluids is seen to decrease by between 4 and 44% as temperature rises from 20℃ to 60℃. Fig. 5 shows that the viscosity of nanofluids increases with increasing particle concentration, and that nanofluid viscosity decreases rapidly as temperature rises. This phenomenon is expected due to the weakening of the inter-molecular and interparticle adhesion forces. Similar behavior has been observed for other nanofluids [24].

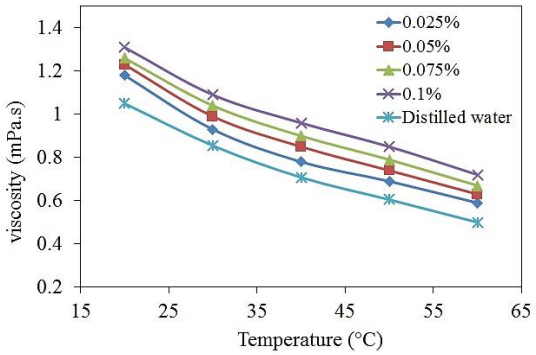

Figure 5 Variation of viscosity of GNP nanofluids with temperature for several GNP concentrations.

Validation

Initially, the experiment is performed for distilled water (DW) as a base fluid and the calculated experimental results are compared to those for the well-known Shah equation.

The results with DW also serve as a baseline for the results using nanofluids [25]. The experimental results are observed in Figure 6 to be in good agreement with Shah's equation, being within a 6.3% error. The Shah equation slightly under-predicts the measurements in the laminar flow regime.

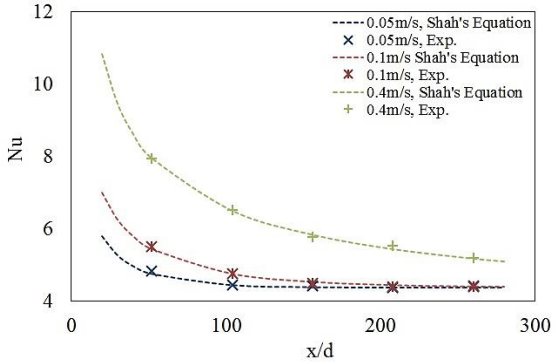

Figure 6 Measured local Nusselt number determined experimentally and with the Shah equation for distilled water, for several velocities.

Friction factors are determined from the measured pressure drops along the length of the test section. To verify the friction factor results, the experimental results for DW are validated by the Hagen–Poiseuille correlation [21]. Figure 7 shows this validation of the experimentally determined friction loss data, demonstrating an error rate of less than 5.4% relative to the Hagen–Poiseuille correlation. Additionally, the friction factor given by f = 64/Re is shown to be accurate within ±6% error.

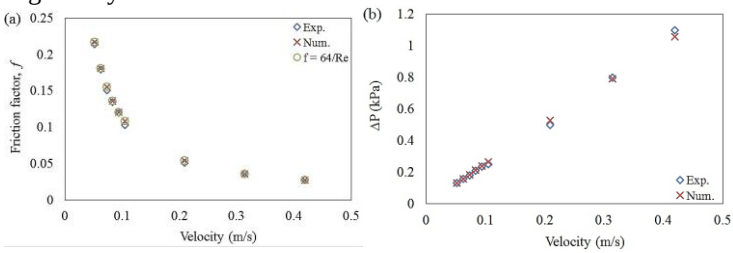

Figure 7. Variation of experimental and correlation data of (a) friction factor and (b) pressure drop of the DW as a function of velocity.

Uncertainty ranges for the measured data and several relevant parameters, obtained using the uncertainty analysis method of Taylor [26] and data reduction processes, are presented in Table 1. The values shown are maximums for the given parameter considering all experimental cases.

Table 1 Uncertainty Ranges for Experimental Data and Results

Parameter	Uncertainty range
Nu_{local}	±7%
h_{ave}	±9%
h_{local}	±10%
f	±10%

RESULTS AND DISCUSSION

Effect of GNP nanoparticle concentration on heat transfer with nanofluids

Based on the literature, the flow characteristics most affecting convective heat transfer are fluid thermal conductivity and velocity [8, 27]. Figure 8 shows the heat transfer coefficient as a function of axial position for various nanofluid concentrations at flow velocities of 005 m/s, 0.07 m/s, 0.1 m/s and 0.4 m/s. Figure 8 also illustrates the variation of convective heat transfer coefficient with non-dimensioned axial distance (x/d), for several fluid velocities. The local heat transfer coefficient is observed to decrease with axial distance, due to an increase in the thermal conductivity of the nanofluid [7]. However, the effect of agglomeration significantly reduces the heat transfer coefficient. The experimental results clearly show that GNP nanofluids enhance the convective heat transfer coefficient and that this enhancement increases with increasing nanoparticle concentration. For instance, the heat transfer coefficient increases from 1% to 15% with an increase in GNP concentration from 0.025wt% to 0.1 wt%.

The enhancement of the local heat transfer coefficient, at x/d~52, is shown in Figure 8 (a) to be 3% for GNP nanofluids containing 0.025 wt% nanoparticles, and 11% at 0.1wt%. But, Figure 8 (d) shows that, although the heat transfer coefficient increases from 3% to 11% at x/d~52, it decreases at x/d~260 by 2% and 11% for the 0.025 wt% and 0.1 wt%, respectively. There are two reasons for the convective heat transfer enhancement of the nanofluids: delay in formation and disturbance of the thermal boundary layers and the high thermal conductivity enhancement of the nanofluid [28]. Additionally, the non-uniform nanoparticle concentration significantly impacts the nanofluid thermal conductivity and viscosity. Based on thermal conductivity theory, the non-uniform thermal conductivity profile is caused by nanoparticle migration and the increase in thermal conductivity normally exceeds the increase in the convective heat transfer coefficient [29]. A heat transfer coefficient enhancement of up to 15% is observed at a velocity of 0.4 m/s and nanoparticle concentration of 0.1wt%, when x/d~52. The agglomeration of nanoparticles may occurs less extensively at low velocity and leads to less significant heat transfer enhancements for nanofluids. However, the agglomeration effect of GNP nanoparticles is reduced at high velocity because the dispersion of nanoparticles increases due to mixing, resulting in an enhanced heat transfer coefficient.

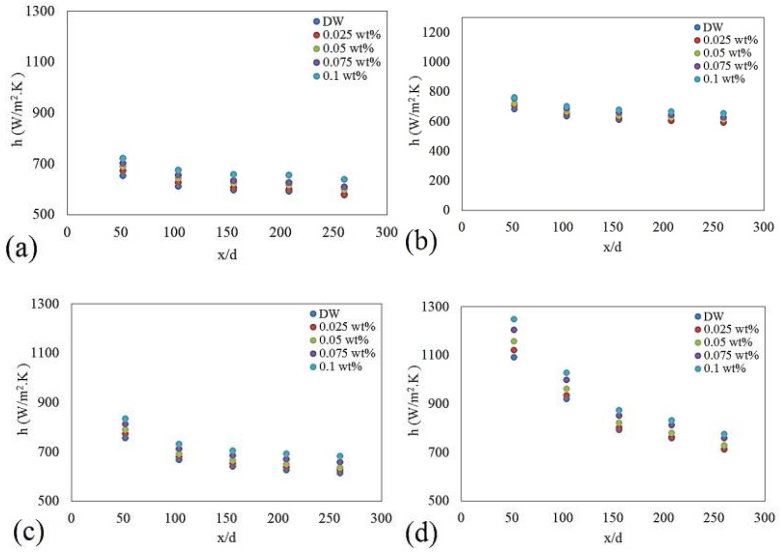

Figure 8 Axial variation of convective heat transfer coefficient for several GNP nanoparticle concentrations and four velocities: (a) 0.05 m/s, (b) 0.07 m/s, (c) 0.1 m/s, (d) 0.4 m/s.

Figure 9 illustrates the relationship between the average convective heat transfer coefficient and velocity for GNP nanofluids of various concentrations. With increasing velocity and concentration, the heat transfer is observed to increase gradually. The coefficient increase for GNP nanofluids is seen to be greater than that for DW, which is attributable to Brownian motion of the nanoparticles, thermal diffusion and thermophoresis [10]. For example, at a velocity of 0.4 m/s, the maximum enhancement of the average convective heat transfer coefficient is about 11% for 0.1wt% GNP nanofluids, but only about 2% for 0.025wt% GNP nanofluids. Adding nanoparticles to the base fluid increases the thermal conductivity of the base fluid, and this effect becomes more pronounced as nanoparticle concentration increases. The thermal conductivity increase enhances the heat transfer performance relative to the base fluid [30]. Hence, raising the concentration of nanofluid and velocity increases the convective heat transfer coefficient.

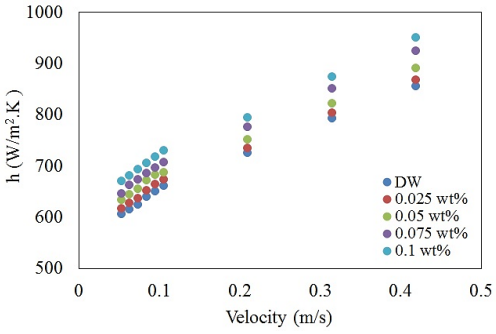

Figure 9 Variation of average heat transfer coefficient with velocity for several GNP nanofluid concentrations.

The variation with velocity of the ratio of heat transfer coefficient of the GNP nanofluid to that of the base fluid, is shown in Figure 10 for several nanofluid concentrations. It is apparent in Figure 9 andFigure 10 that low concentrations of GNP nanoparticles cause quite high enhancements in the heat transfer coefficient. The experimental results suggest that the enhancement in heat transfer coefficient is significant at high velocity. For example, for a 0.025 wt% concentration, the ratio increases from 1.01 to 1.03 as the velocity increases from 0.05 to 0.4 m/s. The greater augmentation is observed for a 0.1 wt% concentration, with a rise in the heat transfer coefficient ratio of 1.11 to 1.15. The augmentation in heat transfer coefficient is caused by the effects of the thermal conductivity enhancement of the base fluid and frequent collisions between the GNP nanosheets, the base fluid and the inner tube wall surface. However, the high specific surface area of the GNP (750 m^2/g) is the another factor that increases the possibility of such interactions [31].

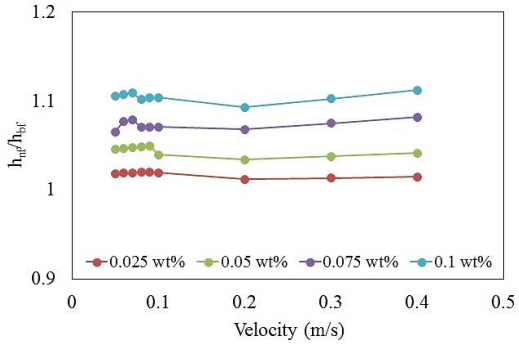

Figure 10 Variation in experimental convective heat transfer for a GNP nanofluid with velocity for several GNP nanofluid concentrations.

Pressure loss

The friction factor of GNP nanofluids flowing through the test section is measured under various conditions including different concentrations and velocities. Figure 11 shows the measured friction factor for the GNP nanofluid for concentrations, as a function of flow velocity. The friction factor of GNP nanofluid is expected to increase due to viscous drag effects and density gradient, based on Equation (5). The results in Fig. 11 show that the friction factor increases with GNP nanoparticle concentration and decreases with velocity. For a fluid flowing through a straight tube, the flow is hydrodynamically fully developed at $x/d \geq \sim 0.05\mathrm{Re}$. For flows with a low Re, the pressure drop is small because the entrance length is small. But the entrance length increases with Re, so the entrance length effect can be significant in some situations.

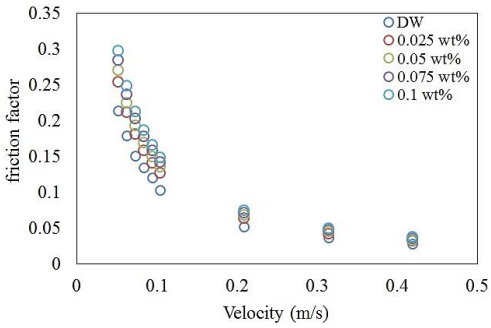

Figure 11 Variation of friction factor of the GNP nanofluid as a function of flow velocity for several GNP nanofluid concentrations.

Thermal performance factor

To evaluate the performance of a nanofluid and to calculate the heat transfer coefficient and Nusselt number (Nu), it is necessary to determine the thermophysical properties of the nanofluid. With these properties and the experimental friction loss, a thermal performance factor of the system can be obtained. The thermal performance factor (η) is defined as follows [6]:

$$\eta = \left(\frac{Nu_{nf}}{Nu_{bf}}\right)\left(\frac{f_{nf}}{f_{bf}}\right)^{1/3} \quad (6)$$

The thermal performance factor is reported in Figure 12 for several nanofluid concentrations. The thermal performance factor of GNP nanofluids relative to the base fluid, is approximately 1 for concentrations of 0.075 wt% and 0.1 wt%. Figure 12 shows that the thermal performance factor increases as GNP nanofluid concentration rises. This phenomena is attributable to the increases of viscosity and thermal conductivity of nanofluids. Increasing the viscosity of a nanofluid reduces the thickness of boundary layer, which results in a heat transfer augmentation, while increasing the thermal conductivity raises the thermal performance factor.

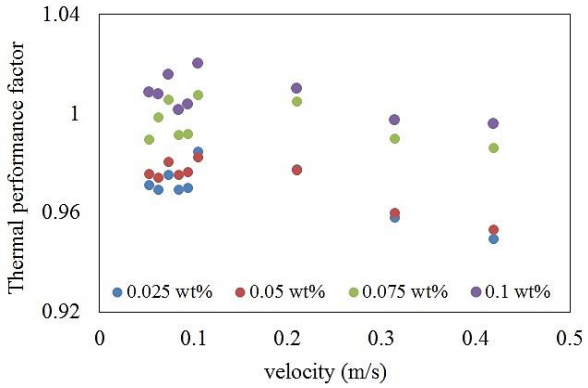

Figure 12 Variation of thermal performance factor with velocity for several GNP nanofluid concentrations.

Entropy generation analysis

The total entropy generation rate ($\dot{E}_{gen}$) for a circular tube of length L is the sum of the thermal entropy generation rate ($\dot{E}_{gen,Th}$) and the frictional entropy generation rate ($\dot{E}_{gen,fl}$), and can be expressed as follows [6]:

$$\dot{E}_{gen} = E_{gen,Th} + E_{gen,fl} \quad (8)$$

$$\dot{E}_{gen,Th} = \frac{\pi d^2 L q''^2}{k_{nf} Nu T_{av}} \quad (9)$$

$$\dot{E}_{gen,fl} = \frac{32\dot{m} f L}{\rho_{nf}^2 \pi^2 d^5 T_{av}} \quad (10)$$

The average temperature of the test section is determined as follows:

$$T_{avg} = \frac{(T_{in} - T_{out})}{\ln\left(\frac{T_{in}}{T_{out}}\right)} \quad (11)$$

The influence of nanoparticle concentration on entropy generation is shown in Figure 13 and Figure 14. The thermal entropy generation rate decreases with concentration and the total and thermal entropy generation decrease with velocity (see Figure 13 (a)). Figure 13 (b) shows that frictional entropy generation increases with GNP nanofluid concentration. Note that the hydrodynamic efficiency of this heat transfer system decreases with GNP nanofluid concentration (even though the rise in frictional entropy is extremely low, and can be neglected).

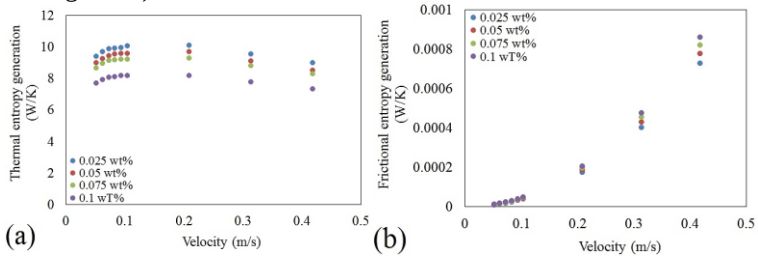

Figure 13 Breakdown of entropy generation rate as a function of velocity for several GNP nanofluid concentrations. (a) Thermal, (b) frictional.

Figure 14 shows that the frictional entropy generation has a minor effect, in the form of a slight reduction, on the total entropy generation because the maximum value of the frictional entropy generation remains less than 1 for all velocities and nanoparticle concentrations. The frictional entropy generation monotonically decreases with velocity, but increases with nanoparticle concentration.

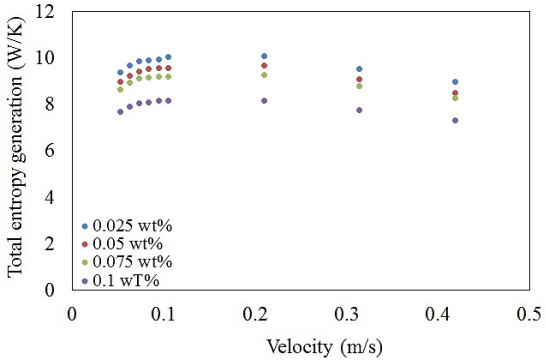

Figure 14 Variation of total entropy generation rate with flow velocity for several GNP nanofluid concentrations.

Increasing the flow velocity from 0.05 m/s to 0.2 m/s causes the total entropy generation to increase, and correspondingly causes the total entropy generation to start to rise. This is because a higher GNP nanofluid concentration enhances heat transfer between the wall and the fluid, reducing the difference between wall and bulk temperatures [32]. Figure 14 and Figure

15 show that the total entropy generation decreases above a velocity of 0.2 m/s and decreases with GNP nanofluid concentration. The main reason for this is the decrease in thermal entropy generation with increasing nanoparticle concentration.

Additionally, the results illustrate that GNP nanofluids can be used as a working fluid in thermal energy systems, with little impact due to increases in fluid viscosity and pressure drop. The results suggest that one can enhance forced convection heat transfer while simultaneously reducing total entropy generation, by increasing GNP nanoparticle concentration.

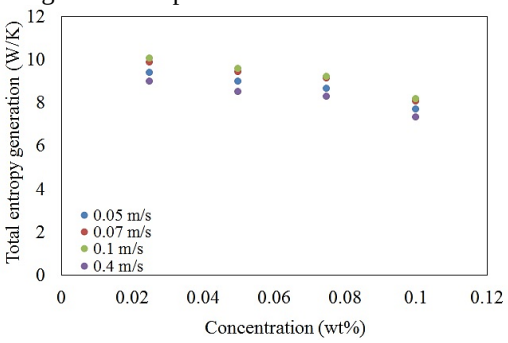

Figure 15 Variation of total entropy generation rate with GNP nanoparticle concentration for several nanofluid velocities.

CONCLUSIONS

The convective heat transfer and flow characteristics of a GNP nanofluid flowing in a horizontal tube has been successfully characterized for laminar flow (bulk velocities ranging from 0.05 to 0.4 m/s, or a Reynolds number varying from 290 to 2,300). Aqueous GNP nanofluids were prepared with four particle concentrations (0.025, 0.05, 0.075, 0.1 wt%) using an ultrasonification probe and were observed to be stable for a long period of time (up to 600 hr). Systematic experiments are performed on the produced GNP nanofluids, for flow through a circular tube, to obtain the convective heat transfer coefficient, friction factor, thermal performance factor and entropy generation. It is found that the effect on heat transfer of GNP thermal conductivity is more significant, on a percentage basis, than the effect of modifying heat transfer coefficient, and that the effect of the GNP nanofluid increases with concentration. This observation is related to the differences in thermal conductivity and heat transfer coefficient, especially the fact that these parameters depend on static and dynamic properties of the GNP nanofluid, respectively. The main conclusions drawn from the study follow:

1. Thermal conductivity increases as nanofluid temperature increases, and the enhancement in thermal conductivity ranges between 12% and 28%.
2. The GNP nanofluid viscosity is strongly dependent on temperature. The viscosity decreases at higher temperatures by 4–44% compared with distilled water.
3. The use of GNP nanofluids increases heat transfer coefficients by up to 15%, and this increase becomes more prominent as velocity and concentration of GNP nanofluid increase.
4. Adding nanoparticles to a base fluid leads to a thermal conductivity enhancement up to 28% and to a heat transfer coefficient increase of up to only 15%. Compared with thermal conductivity theory, a non-uniform thermal conductivity profile results due to particle migration, which raises the convective heat transfer coefficient.
5. An increase in thermal performance can be obtained with GNP nanofluids a factor of up to 1.15. GNP nanofluids at concentrations of 0.075 and 0.1wt% provide a good option for the replacement of conventional working fluids in heat transfer applications.
6. The entropy generation tends to decrease by adding nanoparticles at constant velocity and total entropy generation decreases as velocity rises. However, the increase of velocity and GNP nanofluid concentration causes an increase of frictional entropy generation. This reduces the total entropy generation, but the effect is minor because the maximum value of the frictional entropy generation remains less than 1 for all velocities and GNP nanoparticle concentrations.

As a consequence, it is believed that the GNP nanofluid can be used in many practical engineering applications.

ACKNOWLEDGEMENTS

This research work has been financially supported by the High Impact Research (MOHE-HIR) grant UM.C/625/1/HIR/MOHE/ENG/21, and the University of Malaya in Malaysia.

REFERENCES

[1] M. Mehrali, S.T. Latibari, M. Mehrali, T.M. Indra Mahlia, H.S. Cornelis Metselaar, M.S. Naghavi, E. Sadeghinezhad, A.R. Akhiani, Preparation and characterization of palmitic acid/graphene nanoplatelets composite with remarkable thermal conductivity as a novel shape-stabilized phase change material, Applied Thermal Engineering, 61(2) (2013) 633-640.

[2] M. Mehrali, S.T. Latibari, M. Mehrali, T.M. Indra Mahlia, H.S. Cornelis Metselaar, Preparation and properties of highly conductive palmitic acid/graphene oxide composites as thermal energy storage materials, Energy, 58 (2013) 628-634.

[3] M. Mehrali, S. Tahan Latibari, M. Mehrali, T.M.I. Mahlia, E. Sadeghinezhad, H.S.C. Metselaar, Preparation of nitrogen-doped graphene/palmitic acid shape stabilized composite phase change material with remarkable thermal properties for thermal energy storage, Applied Energy, 135 (2014) 339-349.

[4] M. Goodarzi, M.R. Safaei, K. Vafai, G. Ahmadi, M. Dahari, S.N. Kazi, N. Jomhari, Investigation of nanofluid mixed convection in a shallow cavity using a two-phase mixture model, International Journal of Thermal Sciences, 75 (2014) 204-220.

[5] M.R. Safaei, H. Togun, K. Vafai, S.N. Kazi, A. Badarudin, Investigation of heat transfer enhancement in a forward-facing contracting channel using FMWCNT Nanofluids, Numerical Heat Transfer, Part A: Applications, 66(12) (2014) 1321-1340.

[6] G. Saha, M.C. Paul, Heat transfer and entropy generation of turbulent forced convection flow of nanofluids in a heated pipe,

International Communications in Heat and Mass Transfer, 61 (2015) 26-36.
[7] B.A. Bhanvase, M.R. Sarode, L.A. Putterwar, A. K.A, M.P. Deosarkar, S.H. Sonawane, Intensification of convective heat transfer in water/ethylene glycol based nanofluids containing TiO_2 nanoparticles, Chemical Engineering and Processing: Process Intensification, 82 (2014) 123-131.
[8] P.V. Durga Prasad, A.V.S.S.K.S. Gupta, M. Sreeramulu, L. Syam Sundar, M.K. Singh, A.C.M. Sousa, Experimental study of heat transfer and friction factor of Al_2O_3 nanofluid in U-tube heat exchanger with helical tape inserts, Experimental Thermal and Fluid Science, 62 (2015) 141–150.
[9] Y. Ding, H. Alias, D. Wen, R.A. Williams, Heat transfer of aqueous suspensions of carbon nanotubes (CNT nanofluids), International Journal of Heat and Mass Transfer, 49(1) (2006) 240-250.
[10] L. Zhang, J. Lv, M. Bai, D. Guo, Effect of vibration on forced convection heat transfer for SiO_2–water nanofluids, Heat Transfer Engineering, 36(5) (2014) 452-461.
[11] M. Hemmat Esfe, S. Saedodin, O. Mahian, S. Wongwises, Thermophysical properties, heat transfer and pressure drop of COOH-functionalized multi walled carbon nanotubes/water nanofluids, International Communications in Heat and Mass Transfer, 58 (2014) 176-183.
[12] A.T. Utomo, E.B. Haghighi, A.I.T. Zavareh, M. Ghanbarpourgeravi, H. Poth, R. Khodabandeh, B. Palm, A.W. Pacek, The effect of nanoparticles on laminar heat transfer in a horizontal tube, International Journal of Heat and Mass Transfer, 69 (2014) 77-91.
[13] P.K. Singh, K.B. Anoop, T. Sundararajan, S.K. Das, Entropy generation due to flow and heat transfer in nanofluids, International Journal of Heat and Mass Transfer, 53(21–22) (2010) 4757-4767.
[14] A. Bejan, A study of entropy generation in fundamental convective heat transfer, Journal of Heat Transfer, 101(4) (1979) 718-725.
[15] M.B. Moghaddam, E.K. Goharshadi, M.H. Entezari, P. Nancarrow, Preparation, characterization, and rheological properties of graphene–glycerol nanofluids, Chemical Engineering Journal, 231 (2013) 365-372.
[16] M. Mehrali, E. Sadeghinezhad, S. Tahan Latibari, S.N. Kazi, M. Mehrali, M.N.B.M. Zubir, H.S.C. Metselaar, Investigation of thermal conductivity and rheological properties of nanofluids containing graphene nanoplatelets, Nanoscale Research Letters, 9(1) (2014) 1-12.
[17] M. Mehrali, E. Sadeghinezhad, S. Tahan Latibari, M. Mehrali, H. Togun, M.N.M. Zubir, S.N. Kazi, H. Metselaar, Preparation, characterization, viscosity, and thermal conductivity of nitrogen-doped graphene aqueous nanofluids, Journal of Materials Science, 49(20) (2014) 7156-7171.
[18] K. Novoselov, A.K. Geim, S. Morozov, D. Jiang, Y. Zhang, S. Dubonos, I. Grigorieva, A. Firsov, Electric field effect in atomically thin carbon films, Science, 306(5696) (2004) 666-669.
[19] C.N.R. Rao, U. Maitra, H.S.S.R. Matte, Synthesis, characterization, and selected properties of graphene, in: Graphene: synthesis, properties, and phenomena, Wiley-VCH Verlag GmbH & Co. KGaA, 2012, pp. 1-47.
[20] A. Ghozatloo, A. Rashidi, M. Shariaty-Niassar, Convective heat transfer enhancement of graphene nanofluids in shell and tube heat exchanger, Experimental Thermal and Fluid Science, 53 (2014) 136-141.
[21] K.S. Hwang, S.P. Jang, S.U.S. Choi, Flow and convective heat transfer characteristics of water-based Al_2O_3 nanofluids in fully developed laminar flow regime, International Journal of Heat and Mass Transfer, 52(1–2) (2009) 193-199.

EXPERIMENTAL STUDY ON CAVITY FLOW NATURAL CONVECTION IN A POROUS MEDIUM, SATURATED WITH AN Al_2O_3 60%EG-40%WATER NANOFLUID

C. Grobler[1], M. Sharifpur*[2], H. Ghodsinezhad[2], R. Capitani[2] and J.P. Meyer[2]

[1] Aerospace Systems Competency, Council for Scientific and Industrial Research,
P.O. Box 395, Pretoria 0001, South Africa
[2] Department of Mechanical and Aeronautical Engineering, University of Pretoria,
Pretoria, 0002, South Africa
*Corresponding Author
E-mail: Mohsen.Sharifpur@up.ac.za

ABSTRACT

Natural convection is convection where the fluid motion is driven by buoyancy forces. Porous media and nanofluids have an impact on the heat transfer capabilities of thermal systems. The present experimental study is part of ongoing research and lies at the intersection of buoyancy driven flow in a cavity, porous mediums and nanofluids. The nanofluid consists of Al_2O_3 nanoparticles in the base fluid of 60% ethylene glycol (EG) and 40% water. A Rayleigh number range of $6 \times 10^3 < Ra^* < 1.6 \times 10^4$, for a volume fraction of 0.2% nanoparticles. The porous medium used is glass spheres of 16mm. In this research the effective viscosity of the nanofluid was determined experimentally while the effective thermal conductivity was available in the literature. The results showed that heat transfer is affected by both the porous medium and the nanofluid. The results show that the heat transfer in the case of porous media with nanofluid is more than the case of pure base fluid. However, more experimentation for a wider range of Rayleigh numbers will be a part of future works of this ongoing research.

INTRODUCTION

Convective heat transfer in fluid-saturated porous medium has received much attention in the last few decades and is relevant to a wide range of applications such as underground heat pump systems, solar engineering, packed sphere beds, chemical catalytic converters, heat exchangers and geothermal applications. Extensive reviews of the subject are given in various textbooks for instance, Nield and Bejan [1], Vafai [2], Pop and Ingham [3], Ingham [4] and Bejan et al. [5].

Natural convection inside a porous filled cavity has attracted the attention of many researchers and is very applicable to solar receiver technology. Although more numerical works have been published, a few examples of experimental papers could be found. Prasad et al. [6, 7] presented experimental results for natural convective heat transfer in an annulus. Bories and Combarnous [8] presented numerical and experimental results in a sloping porous layer. The porous medium used was spherical glass beads. Seki et al. [9] presented an experimental study with a rectangular cavity. The fluids included water, transformer oil and ethyl alcohol.

A recent and emerging field, first coined by Choi [10], is the field of nanofluids. The field is based on the premise that suspending solid nanometer sized particles, with higher thermal conductivity, in a conventional heat transfer fluid, would augment the heat transfer capabilities of that fluid. Because nanoparticles could potentially be added to any liquid heat exchangers to augment heat transfer, the potential applications are endless. However, the addition of the nanoparticles to a fluid effects more than its thermal conductivity and different models to predict fluid properties and behaviors have been proposed. Buongiorno [11], Tiwari and Das [12] and Aybar et al. [13].

Free convection of nanofluids in clear cavities with differentially heated walls has been studied both numerically and experimentally. Hwang et al. [14] performed a numerical investigation on a rectangular cavity, following the experimental results presented by Putra et al. [15]. A previous 2D numerical work on Al_2O_3 is also presented by Khanafer et al. [16] Putra et al. [15] performed an experimental investigation of free convection of nanofluids in a horizontal cylinder that is heated from the one side and cooled from the other side. They reported paradoxical results; when the volume fraction was increased, the heat transfer rate was decreased. The work of Putra was extended by an experimental study performed by Nnanna et al. [17] of Al_2O_3 nanoparticles in water. Their focus was to estimate the range of volume fractions for which heat transfer is enhanced. They also wanted to determine the impact of volume fraction on the Nusselt number. They found that for small volume fractions $0.2\% < \phi_{nf} < 2\%$ heat transfer is augmented, but for higher volume fractions, the heat transfer coefficient is reduced due to the reduction of

NOMENCLATURE

Da	[-]	Darcy Number
g	$[m/s^2]$	Gravity Constant
H	[m]	Cavity Height
h	$[W/(m^2 \cdot K)]$	Convective Heat Transfer Coefficient
k	$[W/(kg \cdot K)]$	Conduction Heat Transfer Coefficient
K	$[m^2]$	Permeability
L	[m]	Cavity Length
Nu	[-]	Nusselt Number
Pr	[-]	Prandtl Number
Ra	[-]	Rayleigh Number
T	[K or °C]	Temperature
Special Characters		
β	[1/K]	Volumetric Expansion Coefficient
μ	$[Pa \cdot s]$	Dynamic Viscosity
ν	$[m^2/s]$	Kinematic Viscosity
ρ	$[kg.m^2]$	Density
ϕ	[-]	Nanofluid volume fraction or Porosity depending on the subscript
Subscripts		
bf		Base Fluid
f		Fluid
H		Height
L		Length
nf		Nanofluid
p		Nanoparticle
pm		Porous Medium
s		Solid Matrix

the Rayleigh number. Hu [18] presented experimental and numerical results for natural convection in a square cavity containing TiO_2-water nanofluid. Ho [19] presented an experimental study of Al_2O_3 in water in a vertical square enclosure. Their results are consistent with those found by Nnanna [17].

A further extension to the above mentioned fields is natural convection in porous medium filled cavity, saturated by a nanofluid. This problem has been studied numerically by numerous authors.

Sheremet et al. published a series of papers numerically studying free convection in a porous medium filled cavity saturated by a nanofluid, using Boungiorno's nanofluid model [20–23] or Tiwari and Das' nanofluid model [24, 25].

Grosan et al. 2015 [26] numerically studied this problem, while accounting for internal heat generation as well.

Dastmalchi et al. 2015 [27] presented a study of free convection of Al_2O_3 water nanofluid in a square cavity containing an aluminum porous medium.

Nguyen et al. 2015 [28] numerically studied natural convection of Cu-water nanofluid in a differentially heated non-Darcy porous cavity. The Rayleigh number range studied was $10 < Ra^* < 10^4$ while the solid volume fraction for the medium was $0.4 < \phi_{pm} < 0.9$ and $0\% < \phi_{nf} < 5\%$ for the nanofluid. They found the addition of nanoparticles in the porous medium generally resulted in the higher average Nusselt number in most flow regimes, however the average Nusselt number appeared to decrease with increased solid volume fraction.

The present study is an experimental study, examining buoyancy driven flow of a nanofluid in a square cavity, filled with a porous medium. Literature pertaining to an experimental study of the problem could not be found. The shape of the cavity is square, with two heated vertical walls. The nanoparticles used are Al_2O_3, which is chemically stable in water. While the base fluid is a 60% ethylene glycol (EG) and 40% water mixture, more widely known as antifreeze - a coolant used in many heat exchangers. A Rayleigh number range of $6 \times 10^3 < Ra^* < 1.6 \times 10^4$ and volume fraction of 0.2% particles is studied. The porous medium used is glass spheres of 16mm.

To the best of our knowledge, experimental investigation into natural convective heat transfer of nanofluids in a rectangular cavity filled with a porous medium has not been reported.

THEORY

Analytical Prediction for Heat Transfer

Different heat transfer regimes have been defined for natural convection in a 2D porous rectangular cavity which is heated from the sides. Figure 1 shows under which circumstances each of these heat transfer regimes are applicable. In this study, because the cavity is approximately square, the applicable expected regime is the high Ra regime III. However the cavity in the present experiments has a finite length and 3D effects plays a role.

Nield and Bejan [1] give an analytical prediction for the Nusselt number in the boundary layer Regime based on the Rayleigh number and cavity dimensions. However, this equation is only valid for 2D cavities, and consistently over predicts the Nusselt number.

$$Nu = 0.577 \frac{L}{H} Ra_H^{*1/2} \tag{1}$$

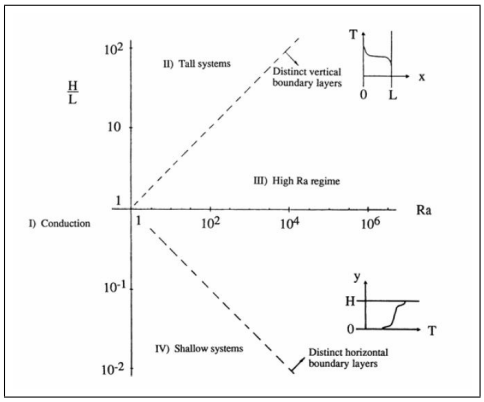

Figure 1: The four heat transfer regimes for natural convection in a two-dimensional porous layer heated from the side [1]

where the Rayleigh number must be based on the height of the cavity. It should also be noted that the equation of the Rayleigh number for a clear cavity (Eq. 2) differs from the one for porous medium (Eq 3) which takes the permeability into account.

$$Ra_L = \frac{g\beta(T_{Hot} - T_{Cold})L^3}{\nu\alpha} \tag{2}$$

$$Ra_L^* = \frac{g\beta(T_{Hot} - T_{Cold})KL}{\nu\alpha_m} \tag{3}$$

In fluid dynamics through porous media, the Darcy number (Da), represents the relative effect of the permeability of the medium versus its cross-sectional area. This can be represented mathematically

$$Da = \frac{K}{d^2} \tag{4}$$

where K[m^2] is the permeability of the medium and d[m] is the particle diameter.

EXPERIMENT AND PROPERTIES

Experimental Setup

Figure 2 shows a schematic of the setup. Opposing vertical walls are heated differentially using nearly constant temperature heat exchangers. Thermocouples are placed along the cavity to measure the temperature distribution inside the cavity. Cavity dimensions are 120.04×96.3×102.3mm (W×H×L). The cavity is placed inside an insulating box with an insulating lid, to prevent heat loss. The thermocouples link to a computer where data is logged.

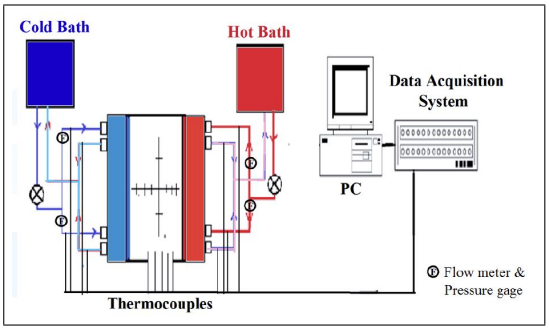

Figure 2: Schematic of Experimental Setup

Experimental Procedure

Nanoparticle dispersion of Al_2O_3 alpha from US Research Nanomaterials is used. The particle size is 30nm and the dispersion is 20wt% (mass fraction) in water. The density of the nanoparticles is given by the US Research Product Fact Sheet [29] at 20°C as 3.5-3.9 g/cm^3.

Before any experimentation could begin, it was first necessary to determine if the nanofluid would remain stable for the duration of the testing. A suspension was prepared and was observed. It was determined to remain stable for at least 24 hours. A new batch of nanofluid was prepared for the experiments, and testing did not exceed 7 hours for four runs.

The dispersion is first diluted in two small batches. The two batches are ultrasonicated, for two hours each. One final mixture is measured, containing the two small batches, diluted in more of the base fluid. This mixture is then ultrasonicated for 3 hours. Ultrasonication breaks up agglomeration of particles in the fluid. The final mixture is a mixture of 60% EG, 40% water as the base fluid with 0.2% volume fraction of nanoparticles suspended.

The cavity was filled with the glass spheres and shaken to ensure good packing. The nanofluid was poured carefully into the cavity, while measuring the amount of fluid used. This is in order to find the porosity of the cavity. The hot and cold baths, as well as the data acquisition system were already switched on. Four runs were recorded as follows:

- The bath temperatures are set for different temperatures as listed in Table 1.
- Steady state is reached at approximately 50 minutes after the start of the run. The last 15 minutes of the data acquisition period (25-40 minutes after steady state is reached) is aggregated as the steady state results.

Table 1: Wall Temperatures

Experiment Number	Hot Wall [°C]	Cold Wall [°C]
1	5	55
2	10	50
3	15	45
4	20	40

Nanofluid Properties

The nanofluid in this study is 0.2% volume fraction of Al_2O_3 in a base fluid of 60%EG-40%water. The particle diameter of the Al_2O_3 is 30nm. The properties of the nanofluid depend amongst others on the type of particles used, the size of particles, the base fluid and the temperature. In all cases temperature was taken into account when material properties were calculated.

Sundar [30] reported conductivity for nanofluid of Al_2O_3 in 60%EG-40%Water, which is used in this study.

According to mixing theory from Ho et al. [19] the density of the nanofluid is given by Equation 5. The density of the Alumina particles is $3900 kg/m^3$.The density of the base fluid at different temperatures is taken from Ashrae Handbook [31].

$$\rho_{nf} = \phi_{nf}\rho_p + (1-\phi_{nf})\rho_{bf} \tag{5}$$

Viscosity of the nanofluid could not be found in the open literature and it was measured as a part of this work and the measurement results can be found in the results section. The viscosity equipment used is a sine-wave vibro-viscometer SV-10 from A&D Company Ltd., Japan, with viscosity measurement limits of 0.3-10,000 mPa.s. More detail on the viscosity measurement is available in our previous publication [32].

The heat capacity is given by Equation 6. [19]

$$\rho_{nf}c_{p,nf} = \phi_{nf}\rho_p c_{p,p} + (1-\phi_{nf})\rho_{bf}c_{p,bf} \tag{6}$$

Ho et al. [19] gives 2 expressions for the coefficient of expansion (β) for a nanofluid. They report that Equation 8 provides a better correlation to experimental results.

$$\beta_{nf} = \phi_{nf}\beta_p + (1-\phi_{nf})\beta_{bf} \tag{7}$$

$$\rho_{nf}\beta_{nf} = \phi_{nf}\rho_p\beta_p + (1-\phi_{nf})\rho_{bf}\beta_{bf} \tag{8}$$

For the base fluid the expansion coefficient was found by numerically finding the derivative of the density to temperature [31], using a central differencing scheme. Ho et al. [19] report the thermal expansion coefficient for alumina nanoparticles is 8.46 $\times 10^{-6}$.

Porous Medium Properties

The medium used is 16mm glass balls. Table 2 presents the material properties of the glass spheres [33].

Table 2: Glass Spheres Material Properties at 20°C

Property Name	Value
Sphere Diameter	16 [mm]
Thermal Conductivity	0.7 [W/(m·K)]
Density	2800 [kg/m^3]
Specific Heat	13.9633 [J/(kg·K)]

Porosity of a medium is measured by volume replacement method and found it equal to 0.429.

Carman-Kozeny relationship is chosen for the Permeability of the medium as

$$K = \frac{D_{p2}^2\phi_{pm}^3}{180(1-\phi)^2} \tag{9}$$

where D_{p2} is dependent on the distribution of sphere diameters. However, in this case all spheres have the same diameters, and as a result $D_{p2} = D_{pm}$. Therefore the Permeability was K = 3.43 $\times$ 10^{-7}m^2.

Different methods are available to determine the effective conductivity of the medium. In this case overall thermal conductivity is used as equation 10 [1]. Unlike porosity and permeability, conductivity is a function of temperature and of the fluid properties. A summary of the medium properties are given in Table 3.

$$k_m = (1-\phi)k_s + \phi k_f \tag{10}$$

Table 3: Porous Medium Properties

Property Name	Value
Porosity	0.429
Permeability	$3.43 \times 10^{-7} m^2$
Conductivity at 0°C	0.490 W/(m·K)
Conductivity at 25°C	0.499 W/(m·K)
Conductivity at 50°C	0.505 W/(m·K)

RESULTS AND DISCUSSION

Nanofluid Viscosity

Figure 3 shows the measured nanofluid viscosity compared to the base fluid. As expected, viscosity of nanofluid is more than the base fluid. However, the difference is more for lower temperatures.

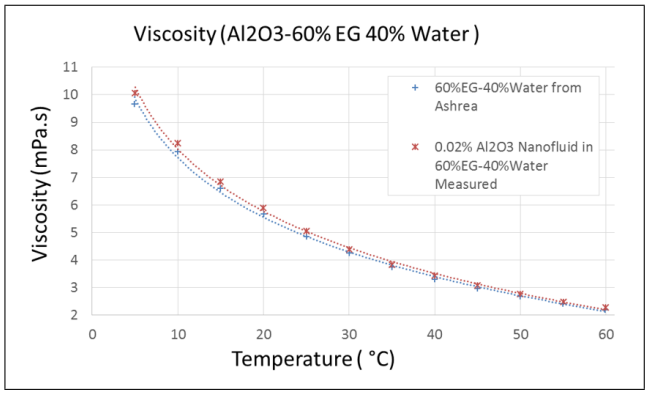

Figure 3: Viscosity of nanofluid vs base fluid

Cavity Experiment

Figure 4 shows the temperature distribution inside the cavity. Thermocouples were approximately equally spaced. From the high gradients close to the hot and cold walls, it is clear that natural convection took place.

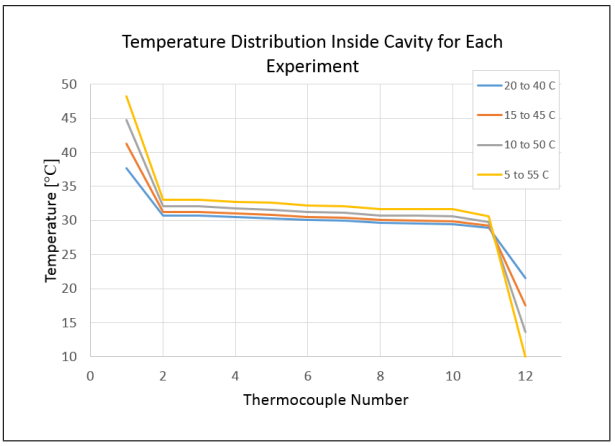

Figure 4: Temperature Distribution inside Cavity

Figure 5 shows the heat transfer for each configuration. Heat transfer was on average 3.5% higher for that of the nanofluid when compared to the base fluid in the porous medium. However, the highest amount of heat transfer was still encountered in the clear cavity (without porous media) and with the base fluid. The heat transfer in the clear cavity, was 6.9% higher than that of the nanofluid in the porous medium.

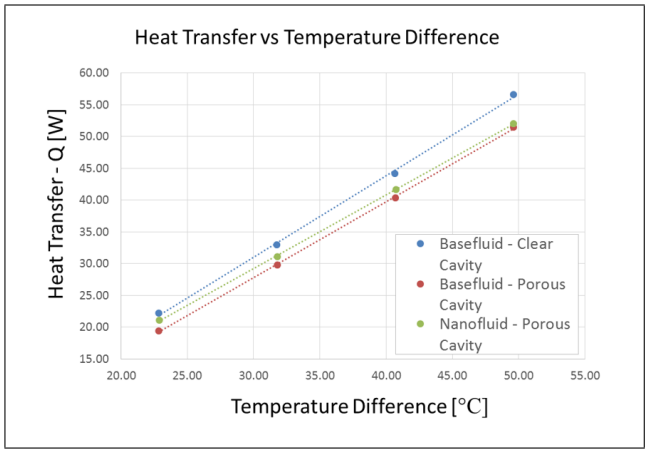

Figure 5: Heat Transfer vs Temperature Difference

Figure 6 & 7 show the clear cavity and porous cavity results for Rayleigh number vs Nusselt number. Logarithmic correlations were extracted from this data. Equations 11, 12 and 13 are respectively the correlations for the base fluid in clear cavity, base fluid in porous filled cavity and nanofluid in porous cavity. However, further works are required to justify the correlations.

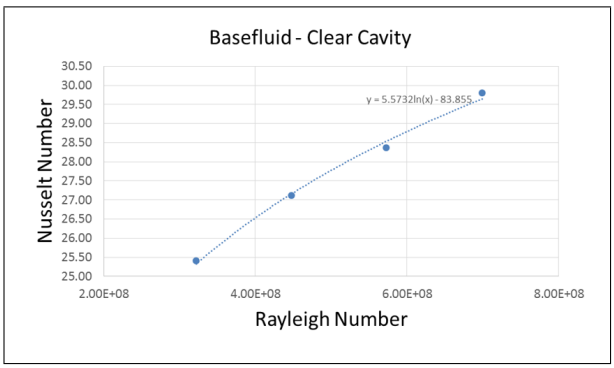

Figure 6: Nusselt vs Rayleigh for Clear Cavity

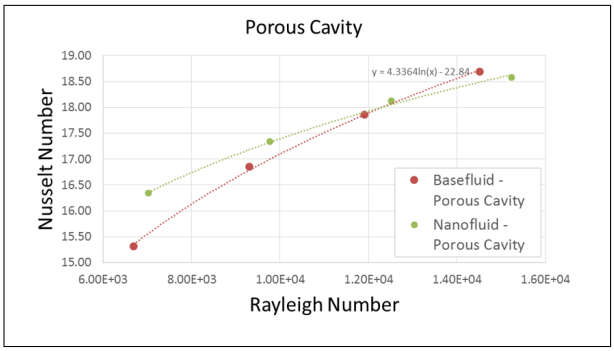

Figure 7: Nusselt vs Rayleigh for Porous Cavity

$$Nu = 5.5732 \ln(Ra_L) - 83.855 \quad (11)$$

$$Nu = 4.3364 \ln(Ra_L^*) - 22.84 \quad (12)$$

$$Nu = 2.9301 \ln(Ra_L^*) - 9.5926 \quad (13)$$

CONCLUSION

Experiments were run to investigate the impact for porous medium and a nanofluid on the heat transfer capabilities a buoyancy driven flow in a differentially heated square cavity. The results showed that heat transfer is affected by both the porous medium and the nanofluid. The clear cavity transferred the most heat and the least heat was transferred by the porous medium saturated with base fluid. Correlations for this range of Rayleigh numbers are developed. Future work will include more experiments in order to extend the range of Rayleigh numbers, Nusselt numbers, and nanofluids used.

ACKNOWLEDGMENTS

The Authors duly acknowledge and appreciate the funding obtained from the following organizations: National Research Foundation of South Africa (NRF), CSIR and EIRT-seed.

REFERENCES

[1] D. Nield and A. Bejan, *Convection in Porous Media*. Springer, 2006.

[2] K. Vafai, *Handbook of Porous Media*. New York: Taylor & Francis, 2005.

[3] I. Pop and D. Ingham, *Convective Heat Transfer: Mathematical and Computational Modeling of Viscous Fluids and Porous Media*. Oxford: Pergamon, 2001.

[4] D. Ingham, *Transport Phenomena in Porous Media III,*. Oxford: Elsevier, 2005.

[5] A. Bejan, I. Dincer, S. Lorente, A. Miguel, and A. Reis, *Porous and Complex Flow Structures in Modern Technologies*. New York: Springer, 2004.

[6] V. Prasad, F. Kulacki, and M. Keyhani, "Natural convection in porous media," *Journal of Fluid Mechanics*, vol. 150, pp. 89–119, 1985.

[7] V. Prasad, F. A. Kulacki, and A. V. Kulkarni, "Free convection in a vertical, porous annulus with constant heat flux on the inner wall - experimental results," *International Journal for Heat And Mass Transfer*, vol. 29, no. 5, pp. 713–723, 1986.

[8] S. A. Bories and M. A. Combarnous, "Natural convection in a sloping porous layer," *Journal of Fluid Mechanics*, vol. 57, no. 1, pp. 63–79, 1973.

[9] N. Seki, S. Fukusako, and I. Inaba, "Heat trannsfer in a confined rectangular cavity packed with porous media," *International Journal for Heat And Mass Transfer*, vol. 21, pp. 985–989, 1978.

[10] S. U. S. Choi, "Enhancing thermal conductivity of fluids with nanoparticles," *Proceedings of the 1995 ASME International Mechanical Engineering Congress and Exposition*, vol. 231, pp. 99–105, 1995.

[11] J. Buongiorno, "Convective transport in nanofluids," *ASME*, vol. 128, 2006.

[12] T. K. Tiwari and M. K. Das, "Heat transfer augmentation in a two-sided lid-driven differentially heated square cavity utilizing nanofluids," *International Journal of Heat and Mass Transfer*, vol. 50, pp. 2002–2018, 2007.

[13] H. Ş. Aybar, M. Sharifpur, M. R. Azizian, M. Mehrabi, and J. P. Meyer, "A review of thermal conductivity models of nanofluids," *Heat Transfer Engineering*, vol. 36, pp. 1085–1110, 2014.

[14] K. Hwang, J. Lee, and S. Jang, "Buoyancy-driven heat transfer of water-based Al2O3 nanofluids in a rectangular cavity," *International Journal of Heat and Mass Transfer*, vol. 50, pp. 4003–4010, 2007.

[15] N. Putra, W. Roetzel, and S. K. Das, "Natural convection of nano-fluids," *Heat and Mass Transfer*, vol. 39, pp. 775–784, 2003.

[16] K. Khanafer, K. Vafai, and K. M. Vafai, "Buoyancy-driven heat transfer enhancement in a two-dimensional enclosure utilizing nanofluids," *International Journal of Heat and Mass Transfer*, vol. 46, pp. 3639–3653, 2003.

[17] A. Nnanna, "Experimental model of temperature-driven nanofluid," *Journal of Heat Transfer*, vol. 129, pp. 697–704, 2007.

[18] Y. Hu, Y. He, S. Wang, Q. Wang, and H. I. Schlaberg, "Experimental and numerical investigation on natural convection heat transfer of TiO_2-water nanofluids in a square enclosure," *Journal of Heat Transfer*, vol. 136, 2014.

[19] C. J. Ho, W. K. Liu, Y. S. Chang, and L. C. C., "Natural convection heat transfer of alumina - water nanofluid in vertical square enclosures: An experimental study," *InternationalJournalofThermalSciences*, vol. 49, pp. 1345–1353, 2010.

[20] M. A. Sheremet and I. Pop, "Natural convection in a square porous cavity with sinusoidal temperature distributions on both side walls filled with a nanofluid: Buongiorno's mathematical model," *Transport Porous Media*, 2014.

[21] M. A. Sheremet and I. Pop, "Natural convection in a wavy porous cavity with sinusoidal temperature distributions on both side walls filled with a nanofluid: Buongiorno's mathematical model," *Journal of Heat Transfer*, vol. 137, 2015.

[22] M. A. Sheremet and I. Pop, "Conjugate natural convection in a square porous cavity filled by a nanofluid using Buongiorno's mathematical model," *International Journal of Heat and Mass Transfer*, vol. 79, pp. 137–145, 2014.

[23] M. A. Sheremet, I. Pop, and M. M. Rahman, "Three-dimensional natural convection in a porous enclosure filled with a nanofluid using Buongiorno's mathematical model," *International Journal of Heat and Mass Transfer*, vol. 82, pp. 396–405, 2015.

[24] M. A. Sheremet, T. Grosan, and I. Pop, "Free convection in a square cavity filled with a porous medium saturated by nanofluid using Tiwari and Das' nanofluid model," *Transport Porous Media*, vol. 106, pp. 595–610, 2015.

[25] M. A. Sheremet, S. Dinarvand, and I. Pop, "Effect of thermal stratification on free convection in a square porous cavity filled with a nanofluid using Tiwari and Das' nanofluid model," *Physica E*, vol. 69, pp. 332–341, 2015.

[26] T. Grosan, C. Revnic, I. Pop, and D. B. Ingham, "Free convection heat transfer in a square cavity filled with a porous medium saturated by a nanofluid," *International Journal of Heat and Mass Transfer*, vol. 87, pp. 36–41, 2015.

[27] M. Dastmalchi, G. A. Sheikhzadeh, and A. A. A. Arani, "Double-diffusive natural convective in a porous square enclosure filled with nanofluid," *International Journal of Thermal Sciences*, vol. 95, pp. 88–98, 2015.

[28] M. T. Nguyen, A. M. Aly, and S. Lee, "Natrual convection in a non-darcy porous cavity filled with Cu-water nanofluid using the characteristic-based split procedure in finite element method," *Numerical Heat Transfer, Part A*, vol. 67, pp. 224–247, 2015.

[29] I. US Research Nanomaterials, "Aluminum oxide (Al2O3) nanopowder water dispersion US7010." Online <http://www.us-nano.com/inc/sdetail/623>, 2014.

[30] L. S. Sundar, E. V. Ramana, M. K. Singh, and A. C. M. Sousa, "Thermal conductivity and viscosity of stabilized ethylene glycol and water mixture Al2O3 nanofluids for heat transfer applications: An experimental study," *International Communications in Heat and Mass Transfer*, vol. 56, pp. 86–95, 2014.

[31] Ashrae, *Ashrae Handbook Fundamentals*. American Society of Heating, Refrigerating and Air-conditioning Engineers, 2009.

[32] S. A. Adio, M. Sharifpur, and J. P. Meyer, "Investigation into effective viscosity, electrical conductivity and ph of γ - Al_2O_3 - glycerol nanofluids in Einstein concentration regime," *Heat Transfer Engineering*, vol. 36, no. 14, 2015.

[33] A. Y. Cengel, *Heat and Mass Transfer: A Practical Approach*. New York: McGraw-Hill, 2006.